Ore Geology Reviews 123 (2020) 103575

Contents lists available at ScienceDirect

Ore Geology Reviews

journal homepage: www.elsevier.com/locate/oregeorev

Geology and geochronology of the Tiegelongnan porphyry-epithermal Cu (Au) deposit, Tibet, China: Formation, exhumation and preservation history

Chao Yang[a,*], Juxing Tang[b], Georges Beaudoin[a], Yang Song[b], Bin Lin[b], Qin Wang[c], Xiang Fang[a,b]

[a] Département de géologie et de génie géologique, Université Laval, Québec, QC G1V 0A6, Canada
[b] MLR Key Laboratory of Metallogeny and Mineral Assessment, Institute of Mineral Resources, Chinese Academy of Geological Sciences, Beijing 100037, China
[c] Chengdu University of Technology, Chengdu 610059, China

ARTICLE INFO

Keywords:
Muscovite
Alunite
^{40}Ar-^{39}Ar
Zircon CA-ID-TIMS
Exhumation
Porphyry-epithermal deposit

ABSTRACT

The Tiegelongnan (Rongna) deposit is a giant porphyry-epithermal Cu (Au) deposit within the Duolong porphyry district, in the south Qiangtang terrane, central-western Tibet, China. The deposit is centered on multiphase granodiorite porphyry (GP) intrusions intruded in Jurassic sandstone. Phase 1 and 2 GP are associated with biotite and sericite alteration, whereas GP3 and 4 occur in middle and shallow parts of the deposit affected by sericite and advanced argillic alteration (alunite-kaolinite-dickite-pyrophyllite). Sericite alteration is pervasive in the deep part of the deposit replacing biotite alteration and hosting porphyry stage chalcopyrite-bornite-pyrite ± molybdenite mineralization. Advanced argillic alterationis associated with epithermal stage high sulfidation (tennantite, enargite, bornite, and digenite) mineralization, overprints the sericite and biotite alteration from the shallow part of the deposit. The top of the Tiegelongnan hydrothermal system was weathered with a layer of supergene oxidation and enrichment zone, exhumated, and covered by andesite and gravel.

Muscovite sampled from deep sericite alteration yields a ^{40}Ar-^{39}Ar age of 120.9 ± 0.8 Ma, which is consistent with previously reported hydrothermal biotite ^{40}Ar-^{39}Ar age of 121.1 ± 0.6 Ma, molybdenite Re-Os ages of 121.2 ± 0.6 and 119.0 ± 1.4 Ma, and GP 1 and 2 zircon U-Pb ages of 121.5 ± 1.5, 120.2 ± 1.0 Ma (LA-ICP-MS results), and 118.7 ± 0.9 Ma (SIMS result). Phase 3 GP 3 yields a CA-ID-TIMS zircon U-Pb age of 119.9 ± 0.2 Ma, which constrains the age of porphyry magmatic-hydrothermal events. The porphyry system was then unroofed, weathered, and superimposed by discrete stages of advanced argillic alteration and high sulfidation mineralization. Two pulses of alunite events yield ^{40}Ar-^{39}Ar ages of 116.3 ± 0.8 Ma and 111.7 ± 1.0 Ma, which represent the principal epithermal alteration and mineralization ages at Tiegelongnan. The first alunite pulse age is consistent with younger porphyry (GP4) age of 116.2 ± 0.4 Ma (zircon LA-ICP-MS age). Weathering and exhumation of the porphyry-epithermal deposit were continuing until the cover of andesite at ~110 Ma and by post-andesite gravel. The andesite was affected by a younger weak hydrothermal alteration at 108.7 ± 0.7 Ma, constrained by a muscovite ^{40}Ar-^{39}Ar age. Another barren alunite yields a ^{40}Ar-^{39}Ar age of 100.6 ± 2.0 Ma, which may represent the youngest hydrothermal event. The long life-span discrete hydrothermal activities from ~120 to ~100 Ma in the Tiegelongnan deposit is consistent with the long-lasting tectonic-magmatic events of the Bangong-Nujiang suture zone.

The discrete epithermal mineralization events at Tiegelongan are younger than the porphyry mineralization events, which is analogous to several other epithermal deposits worldwide. The ~10 m.y exhumation history at Tiegelongan is slower than the typical and rapid erosion history of ~1–2 m.y porphyry deposits in low-altitude tropical climates regions, and during a specific abrupt uplift pulse in the Andean region. The slow exhumation at Tiegelongnan is interpreted to be an integrated result of an arid climate environment, relatively flat topography, and a slow uplift condition during Cretaceous in central-western Tibet.

1. Introduction

Porphyry deposits and their overlying epithermal hydrothermal systems are attractive exploration targets, particularly for Cu, Mo, and Au (Hedenquist and Arribas, 2000; Sillitoe and Hedenquist, 2003). Epithermal deposits have been mostly recognized as precious metal gold resources (Cooke and Simmons, 2000), whereas some epithermal base metal mineralizations have also been reported (Fontboté and

* Corresponding author.
E-mail address: chaoyangcn8@gmail.com (C. Yang).

https://doi.org/10.1016/j.oregeorev.2020.103575
Received 4 October 2019; Received in revised form 16 April 2020; Accepted 4 May 2020
Available online 05 May 2020
0169-1368/ © 2020 Elsevier B.V. All rights reserved.

Bendezú, 2009). Some epithermal deposits are found as isolated deposits, such as the Summitville deposit, USA (Stoffregen, 1987; Gray and Coolbaugh, 1994), and the Pascua-El Indio epithermal belt, Argentina and Chile (Chouinard et al., 2005; Deyell et al., 2005b). Under most cases, epithermal mineralization is found telescoped on porphyry mineralization (Sillitoe, 1999), such as the Zijinshan, China (So et al., 1998; Jiang et al., 2013), Oyu Tolgoi, Mongolia (Perelló et al., 2001), Cerro la Mina, Mexico (Jansen et al., 2017), and La Bodega and La Mascota, Colombia (Madrid et al., 2017). In other situations, the overlying epithermal system was eroded, displaced, or tilted from the porphyry system, which results in that epithermal deposits are not always present with porphyry deposits (Garwin et al., 2005; Seedorff et al., 2005; Kesler and Wilkinson, 2006).

The duration of porphyry-related magmatic-hydrothermal systems was reported to last up to several million years, as results of intermittent, successive stages of magmatic and hydrothermal events (Parry et al., 2001; Sillitoe and Moretensen, 2010; Maydagán et al., 2014; Mercer et al., 2015). In contrast, the formation duration of a single event of porphyry mineralization is theoretically modeled to range from < 2000 to < 100,000 years, (Cathles et al., 1997; McInnes et al., 2005; Cathles and Shannon, 2007). Epithermal and porphyry alteration are interpreted to form simultaneously at two endmembers (vapor and brine) of phase-separated magmatic water (Arribas, 1995; Hedenquist et al., 1998). However, when multistage epithermal mineralization formed, some pulses of the epithermal event are not necessarily associated with the nearby porphyry, being younger than the porphyry event (Catchpole et al., 2015; Correa et al., 2016; Madrid et al., 2017).

There are few epithermal deposits discovered in Tibet, in contrast to a number of porphyry deposits been reported in the Gangdese and Yulong belts (Fig. 1a) (Hou et al., 2011; Tang et al., 2012; Mao et al., 2014). This study reports the geology and geochronology of the high sulfidation epithermal mineralization telescoped on porphyry mineralization at the Tiegelongan, also named as Rongna deposit by Zhang et al. (2018), Tibet, China. Based on cores logging, we complement with new zircon U-Pb and multiple stages of muscovite and alunite ^{40}Ar-^{39}Ar ages, to reveal the long life span and multiple stages of hydrothermal activity, and to illustrate the formation, exhumation, and preservation history at the Tiegelongnan deposit.

2. Exploration history

Mineral exploration in the Duolong region began in the 1980s with the discovery of some old placer gold stope relics. The main exploration objectives focused on the placer gold mines until 1998. After that, the No.5 Geological Party in Tibet conducted a geological survey and found evidence for copper and gold potential. In 2003, two porphyry Au-Cu deposits, Duobuza and Bolong were discovered. The exploration at the Tiegelongnan commenced in 2010 by No. 5 Geological Party of Tibet, and soil geochemical Cu and Au anomaly were found in an oxidation zone (Fig. 2). Four shallow holes were drilled in the following three years at the anomaly area. However, these drill holes were offset from the center of the Tiegelongnan ore-body, which is under the volcanic andesite cover. In 2012, Chinalco Jinlong Company partnered with the No.5 geological party and the Institute of Mineral Resources of the Chinese Academy of Geological Sciences to extend the scope of exploration, based on the regional geochronological indication that andesite is younger than the ore-related porphyritic intrusions. They sunk diamond drill-holes to the east of original drill holes at Tiegelongnan, passing through the andesite cover (Fig. 2), to discover the Tiegelongan deposit in 2013 (Tang et al., 2014).

3. Duolong porphyry deposit district

The Duolong porphyry Cu-Au deposit district is located ~30 km north of the Bangong–Nujiang Suture Zone (BSZ) within the southern margin of South Qiangtang sub-terrane (Fig. 1a), at an elevation from 4700 to 5200 m, in a 47 km long by 21 km wide area. This region is located in a continental arc related to the northward subduction of the Bangong-Nujiang Ocean (BNO) (Li et al., 2014; Li et al., 2019). Porphyry deposits in this belt were formed during the Early Cretaceous, but it remains controversial whether they formed during the subduction stage (Li et al., 2016b, 2017a, 2017b), or post-subduction collisional stage (Zhu et al., 2016; Liu et al., 2017; Wei et al., 2017).

The Duolong district contains measured and inferred resources of 17.54 Mt Cu and 374.2 t Au in four well-explored deposits, Duobuza, Bolong, Naruo, and Tiegelongnan (Fig. 1b). Duobuza was the first porphyry Au-Cu deposit discovered in this district with 648 million tonnes (Mt) resources at grades of 0.46% Cu and 0.20 g/t Au. The Bolong porphyry Cu-Au deposit contains 640 Mt ore averaging 0.43% Cu and 0.23 g/t Au. The Naruo porphyry Cu-Au deposit, characterized by breccia ore-body, contains 660 Mt with an average 0.38% Cu, and 443 Mt of ore with average 0.19 g/t Au (Li et al., 2013; Ding et al., 2017; Lin et al., 2018). Tiegelongnan is the largest porphyry and epithermal deposit, containing 2089 Mt ore at a grade of 0.53% Cu and 0.08 g/t Au (Tang et al., 2017). There are other porphyry and epithermal related mineralization prospects in this district, including the Nadun high sulfidation epithermal Cu-Au deposit with 0.14 Mt ore at 0.75% Cu and 1.45 g/t Au (Li et al., 2016a), Dibao, Saijiao, Sena porphyry related mineralization, and Gaerqin epithermal mineralization (Fig. 1b). All these deposits are associated with Cretaceous subvolcanic porphyry intrusions between 128 and 114 Ma (Fig. 1b; Li et al., 2011; Lin et al., 2017a; Sun et al., 2017; Zhang et al., 2017). Most of those intrusions are intermediate to felsic porphyry rocks, such as diorite, quartz diorite, and granodiorite porphyry rocks. Quartz diorite and granodiorite porphyries are the main intrusion types associated with the Cu-Au mineralization, but differing in some deposits, with granodiorite porphyry in Naruo (Ding et al., 2017), Bolong (Zhu et al., 2015) and Tiegelongnan deposit (Lin et al., 2017b), and quartz diorite and granodiorite porphyry in Duobuza (Li et al., 2012). All those porphyry rocks are oxidized, water-rich, and subduction-related calc-alkaline magmas (Li et al., 2016b; Sun et al., 2017). Previous data indicate that porphyritic intrusions emplaced between 120 and 118 Ma, and the hydrothermal alteration and mineralization formed between 122 and 115 Ma, which was followed by post-mineral volcanic rocks erupted between 113 and 106 Ma (Fig. 1; Wang et al., 2015; Li et al., 2016b, 2017b; Lin et al., 2017a). The volcanic rocks consist of basalt, andesite, dacite, rhyolite, and voluminous pyroclastic rocks. Andesitic rocks are the most widespread volcanic units, which belong to the Cretaceous Meiriqiecuo Formation. All those volcanic rocks are cogenetic to the porphyritic intrusions, indicated by their close spatial and temporal relationship, and geochemical signatures (Li et al., 2016b; Sun et al., 2017).

Most of those deposits and igneous rocks are spread along NE and SW faults (Fig. 1b). The NE striking faults are recognized to control the locations of magmatic-hydrothermal events, whereas the W-E striking faults are post-mineral structures that cut the ore bodies (Song et al., 2018).

The oldest sedimentary rock in the Duolong district is the limestone of the Upper Triassic Riganpeicuo Formation. It is overlain by the widespread Upper to Middle Jurassic Sewa and Quse Formation sandstone, siltstone, and claystone, which are the main wall-rocks for all the deposits in the Duolong district. The Oligocene Kangtuo Formation conglomerate overlies the Jurassic sedimentary rocks, and is unconformably overlain by the Quaternary eluvial sediments.

4. Deposit geology

The Tiegelongnan deposit is hosted by Jurassic Sewa Formation submarine sandstone and siltstone and granodiorite porphyry intrusions. A small portion of biotite hornfels is revealed by several deep diamond drill holes, surrounding the deep porphyry intrusions (Fig. 3b). Fractures in hornfels are filled by irregular, barren, and

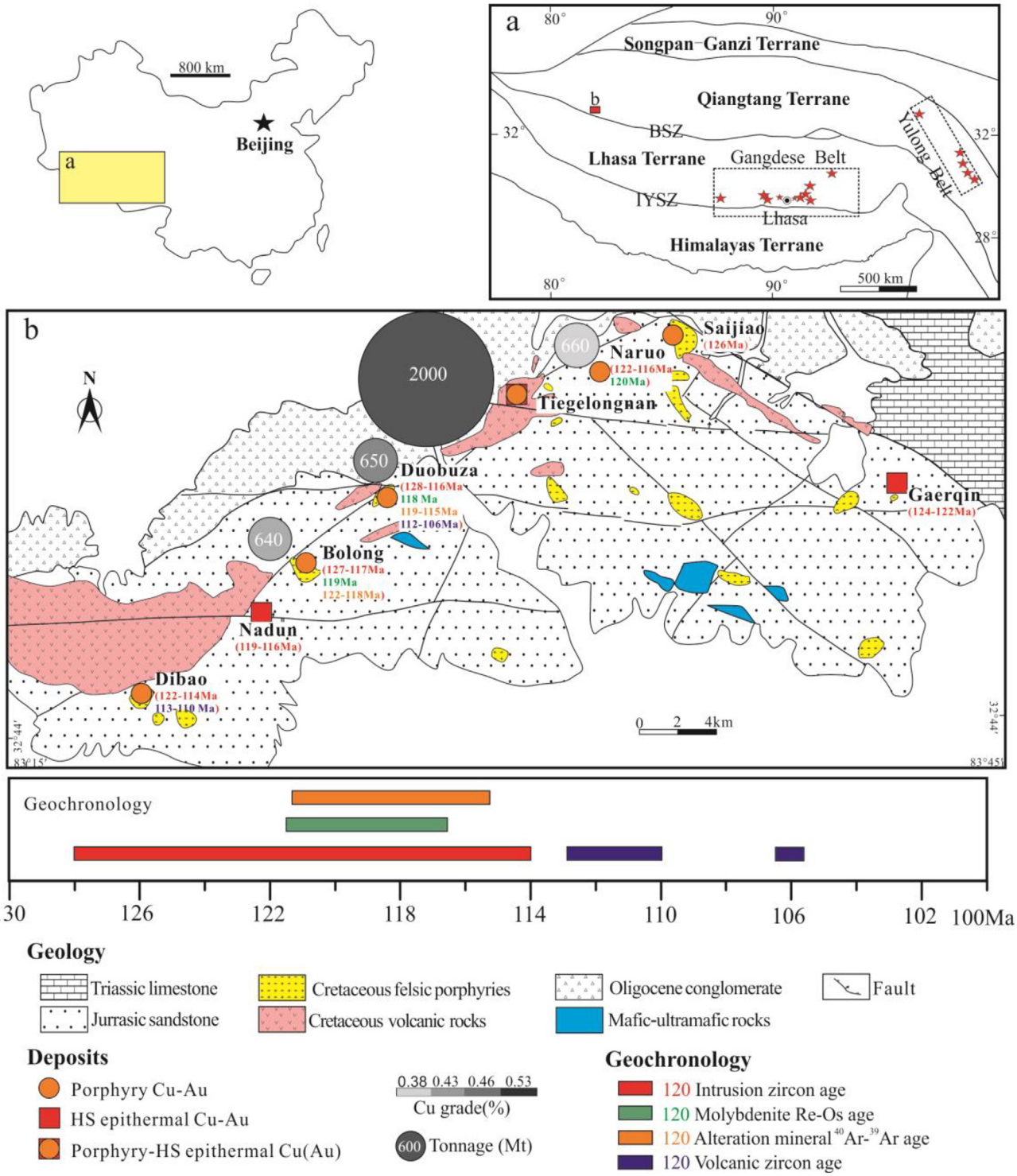

Fig. 1. Geology and geochronology frame of the Duolong district. BSZ, Bangong-Nujiang Suture Zone. IYZ, Indus-Yaluzangbu Suture Zone. HS, high-sulfidation. Geochronology data for Dibao, Duobuza, Bolong after Lin et al. (2017a), data for Naruo from Ding et al. (2017) and Lin et al. (2018), data for Nadun from Li et al. (2016a, 2016b), data for Gaerqin from Zhang et al. (2017).

narrow quartz veins (< 2 mm wide).

Several diorite porphyry dikes are found in the eastern and southern part of the deposit, which is affected by chlorite alteration with few hypogene chalcopyrite and supergene chalcocite mineralizations (Fig. 3). They are isolated from several phases of granodiorite porphyry intrusions (Fig. 3), and no crosscutting relation is observed between diorite and granodiorite porphyries. Subdivision of those granodiorite porphyry intrusions is difficult because hydrothermal sericite alteration masks the original features. Zhang et al. (2018) also named some intrusions as “feldspar porphyry”. Phenocrysts, mineral type and proportion, vein types and density, and enclaves are used to distinguish different granodiorite porphyry phases and their sequence, which are summarized in Table 1 and Fig. 4. Granodiorite porphyry 1 (GP 1), occurring at depth in the Tiegelongnan deposit, contains biotite phenocrysts with more feldspar than quartz phenocrysts (Fig. 4a), and is cut by the highest density quartz-molybdenite veins compared to the

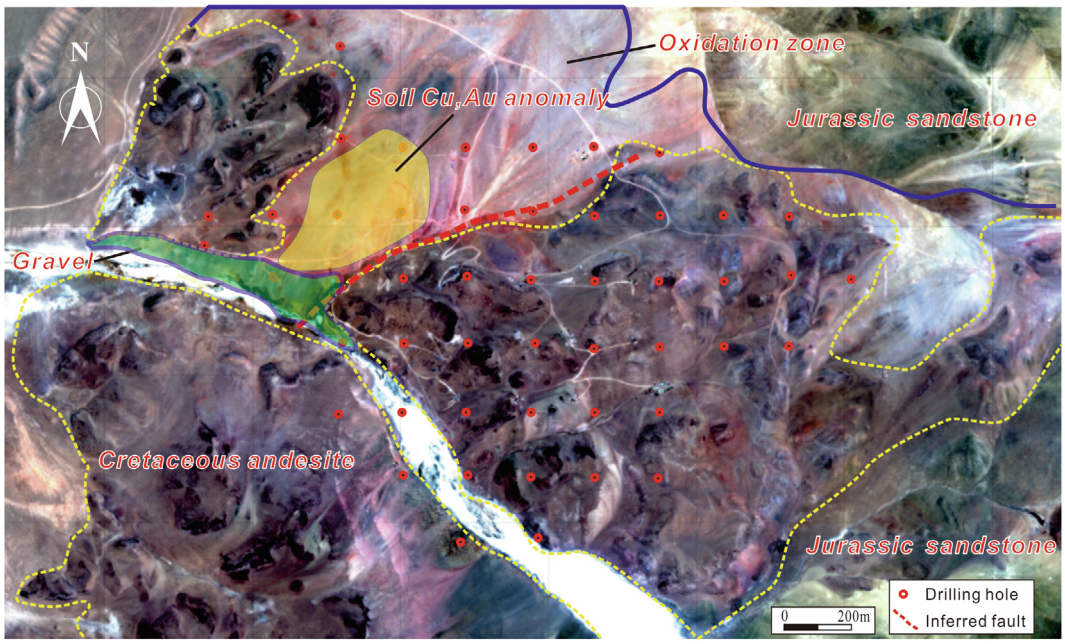

Fig. 2. Satellite photo of the Tiegelongnan deposit. Most of the drill holes pass through the andesite cover, which overlies the Jurassic sandstone hosting ore body. Soil Cu, Au anomaly zone was first recognized as an exploration potential prospects for this deposit.

other porphyry phases. Granodiorite porphyry phase 2 (GP 2) is the most common intrusion type, it contains a higher proportion of phenocrysts than GP 1 (55–60% for GP2 and 35–40% for GP1), with more feldspar (25–30%) than quartz (15–20%) (Fig. 4b). Magmatic GP 2 breccias occur at depth in the center of the deposit (Fig. 3b). Few biotite hornfels clasts are found in GP 1 and GP 2 porphyries, which suggests biotite hornfels formed before the intrusions. GP 2 is strongly affected by sericite alteration and disseminated chalcopyrite, bornite, and some molybdenite mineralization, and cut by minor quartz-molybdenite veins and quartz-pyrite ± chalcopyrite ± bonite veins (Fig. 4c). Granodiorite porphyry 3 (GP 3) dikes are found in the shallow part of Tiegelongnan with a lower proportion of phenocrysts (25–35%), and less feldspar (5–8%) than quartz (15–20%) phenocrysts compared to GP 1 and GP 2 porphyries (Fig. 4d, e). They contain disseminated high sulfidation sulfide assemblage characterized by digenite, bornite, enargite, and tennantite, cut by digenite-bornite-pyrite veins (Fig. 4d). GP 3 dikes are considered younger than GP 2 because they have GP 2 clasts and lack earlier chalcopyrite, bornite, and molybdenite sulfide assemblages (Fig. 4e). Granodiorite porphyry 4 (GP 4) is found in the middle and western parts of the deposit (Fig. 3). The GP4 contains more phenocrysts (40–50%) than GP 3, and more quartz (25–30%) than feldspar (5–10%) phenocryst (Fig. 4f), which differs from GP 1 and GP 2. The GP 4 is mineralized with disseminated digenite and bornite, and cut by bornite-digenite-pyrite veinlets (< 0.5 cm wide).

The top of GP 3 dikes are unroofed (Fig. 3b and c), which suggests the uplifting and erosion happened after the emplacement of these intrusions. Few meters thick layers of erosional breccia are found at the top of the mineralized rocks, which reaches tens of meters in the southern part (Fig. 3b and c). The erosional breccia is associated with supergene oxidation (Song et al., 2018), where the erosional breccia, including quartz clasts, sandstone, and porphyry clasts, are cemented by jarosite, goethite, and hematite.

5. Post-mineral units

5.1. Andesite cover

The Tiegelongnan deposit is largely covered by andesite, with small amounts of mafic rocks (Figs. 2 and 3). Oxidized wall rocks, kaolinite breccia, porphyry clasts are found in andesite. Most of the andesite cover is unaltered and lack sulfide minerals. A small portion of the middle south-eastern part of the andesite is weakly altered with chlorite, and cut by calcite and kaolinite veins (Fig. 5a). This part of andesite occurs as hydrothermal breccia cemented by kaolinite (Fig. 5b). The andesite cover is cut by a WNW striking reverse fault, which dips steeply to the south, and uplifts the andesite hanging wall in the southern part of this deposit, (Fig. 3c).

5.2. Gravel

The andesite cover is discontinuous at the western part of the Tiegelongnan deposit, where a thin layer (< 1 m) of piedmont and stream gravel unconformably overlies the deposit (Figs. 2 and 5c). It thickens to the southern end, where the gravel contains andesite clasts (Fig. 5d) with a thickness of ~10 m.

6. Alteration and mineralization

We integrate > 200 thin section descriptions and X-ray Diffraction (XRD) in this study with summary of short wave inferred spectrum (SWIR) results (Guo et al., 2017) and previous alteration and mineralization description (Yang et al., 2014; Lin et al., 2017b), to describe the alteration mineralogy, texture, and their distribution in the Tiegelongnan deposit based on over 20 km cores logging in the field.

Spatial distribution pattern of alteration is shown in Fig. 6. Sericite alteration is present at depth and in the eastern shallow part from depths of 150 m to 1200 m. Chlorite alteration occurs in the south-eastern periphery of the sericite alteration zone in a propylitic halo. Advanced argillic alteration, consisting of kaolinite-dickite and alunite alteration zones, is found below a depth of ~200 m, and overprints the sericite alteration and chlorite alteration.

6.1. Biotite alteration

Hydrothermal biotite is identified in the deep, central parts of the Tiegelongan, below 900 m depth (Yang et al., 2014; Lin et al., 2017b). Biotite occurs with chalcopyrite in quartz veins, and in quartz-molybdenite-chalcopyrite-pyrite veins. Biotite is commonly replaced by

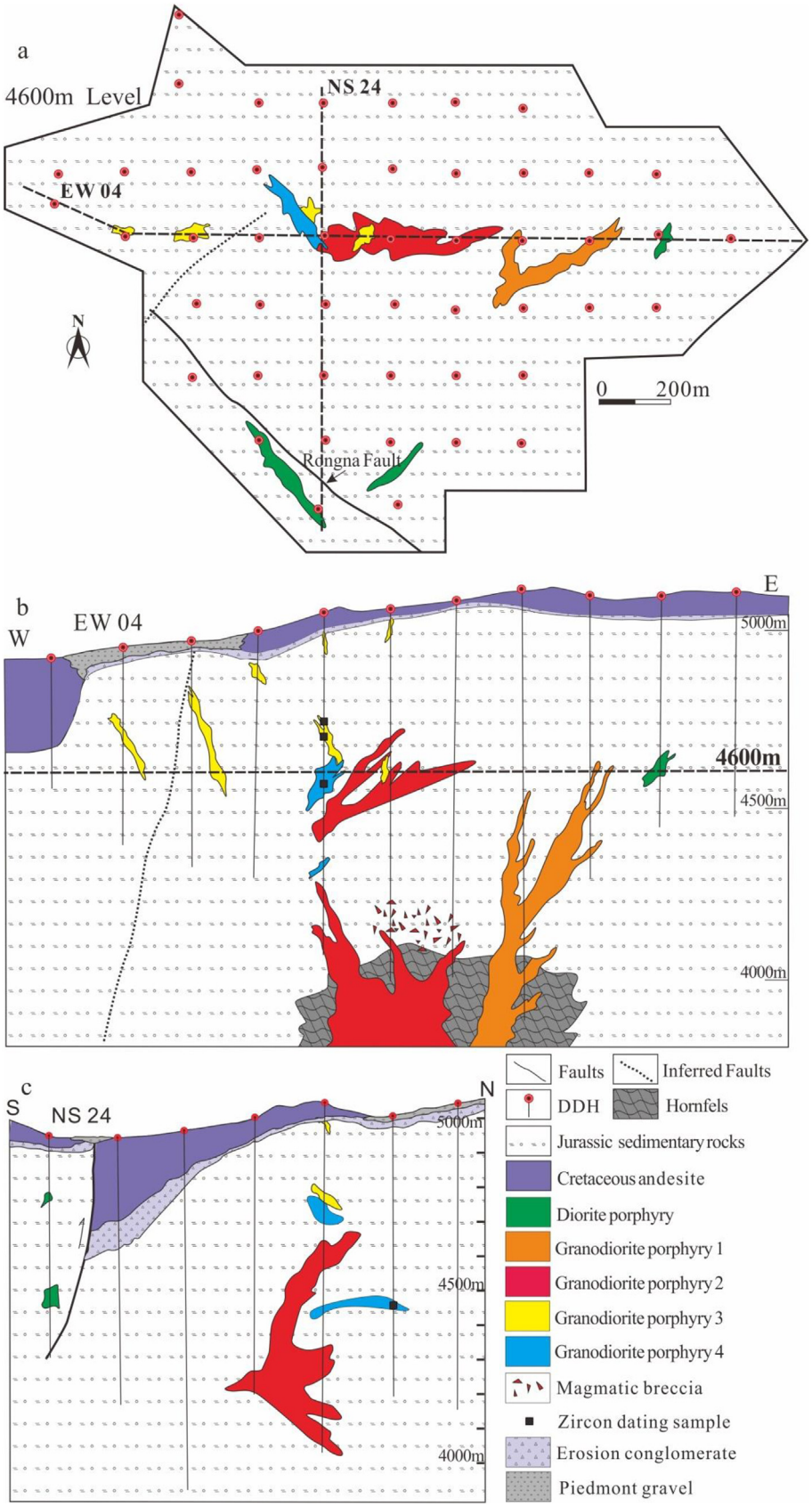

Fig. 3. Geology of the 4600 m elevation level (a), cross-section EW 04 (b) and cross-section NS 24 (c) of Tiegelongnan deposit.

Table 1
Features of different phases of granodiorite porphyry.

Rock types	Pheno (%) and composition	Trapped clasts	Veins	Mineralization	Zircon U-Pb age (Ma)
Diorite porphyry	40–50%: 25% Fel 0.5–4 mm; 2% Qt 0.5–2 mm; 20% Hen 1–3 mm	No	Chl-Py vein	Intermediate mineralization Minor Cc, Py	123.1 ± 1.7[1]
Granodiorite porphyry 1	35–40%: 20–25% Fel 1–8 mm; 5–10% Qz 0.5–4 mm; 10–15% Bt 0.5–10 mm	Rare sedimentary clasts	Qz-Mol ± Ccp vein	Intermediate: Mol, Ccp, Py	121.5 ± 1.5[1]
Granodiorite porphyry 2	55–60%: 25–30% Fel 0.5–5 mm; 15–20% Qz 0.5–3 mm; 6–8% Bt/Hen 1–4 mm	Rare sedimentary clasts	Qz-Mol ± Ccp vein Qz-Ccp-Py ± Bn vein Bn-Dg-Py vein	Strong: some amount of Mol, Ccp, Bn, Py, and minor Cv, Tnt, Eng	120.2 ± 1.0[2]
Granodiorite porphyry 3	25–35%: 5–8% Fel 0.5–4 mm; 15–20% Qz 0.5–3 mm; 3–5% Bt/Hen 0.5–3 mm	With some earlier intrusions clasts	Bn-Dg-Py vein	Weak: Bn, Dg, Py	119.9 ± 0.2
Granodiorite porphyry 4	40–50%: 5–10% Fel 0.5–4 mm; 25–30% Qz 0.5–2.5 mm; 1–4% Bt/Hen 0.5–2 mm	Hydrothermal breccia	Bn-Dg-Py vein	Intermediate: Dg, Bn, Ccp, Py and minor Eng, Tnt,	116.2 ± 0.4

Bn-bornite, Cc-chalcocite, Ccp-chalcopyrite, Chl-chlorite, Cv-covellite, Dg-digenite, Eng-enargite, Fel-feldspar, Mol-molybdenite, Py-pyrite, Qz-quartz, Tnt-tennantite.
1 – Lin et al., 2017b, 2 – Fang et al., 2015.

muscovite and kaolinite (Lin et al., 2017a, Fig. 5e). Several types of quartz veins are identified and named based on the classification of (Gustafson and Hunt, 1975). Early barren quartz veinlets are cut by mostly B-type (molybdenite-bearing) veins and by minor A-type (chalcopyrite-bearing) veins in the biotite alteration zone.

6.2. Sericite alteration

Sericite alteration is generally centered on almost all granodiorite porphyry dikes. Granodiorite porphyries and their vicinity sandstone host rocks have been altered by muscovite-quartz-pyrite assemblage with minor other hydrothermal minerals, and cut by several types of quartz-bearing veins (Table. 2). Feldspar minerals are mostly altered to muscovite, with coeval precipitation of disseminated chalcopyrite, bornite, and pyrite (Fig. 7a). Few magnetite, hematite, tourmaline, phengite, and barite are present in the sericite alteration zone. Rutile is common as disseminated grains and in quartz veins. Gypsum occurs in quartz veins in the sericite alteration zone. Pyrophyllite (Fig. 7d) is identified with minor dickite in the shallow sericite alteration zone.

A-type vein comprising chalcopyrite with varying amounts of bornite rarely occur in deep sericite alteration zone, which is cut by molybdenite-bearing B-type veins and pyrite veins (Fig. 7b). B veins they are cut by D-type pyrite-bearing quartz veins, and then cut by younger pyrite veins (Fig. 7c). Reopening of the quartz vein is commonplace, where younger kaolinite, alunite, and sulfide minerals fill their open void. Minor galena and sphalerite occur in A-type veins with chalcopyrite and bornite, some of which are replaced by younger covellite, digenite, enargite, and tennantite.

6.3. Chlorite alteration

Chlorite alteration is characterized by an assemblage of chlorite-epidote-calcite-pyrite (Table 2). Chlorite replaces feldspaths in sedimentary rocks, and mafic minerals in diorite porphyry, and

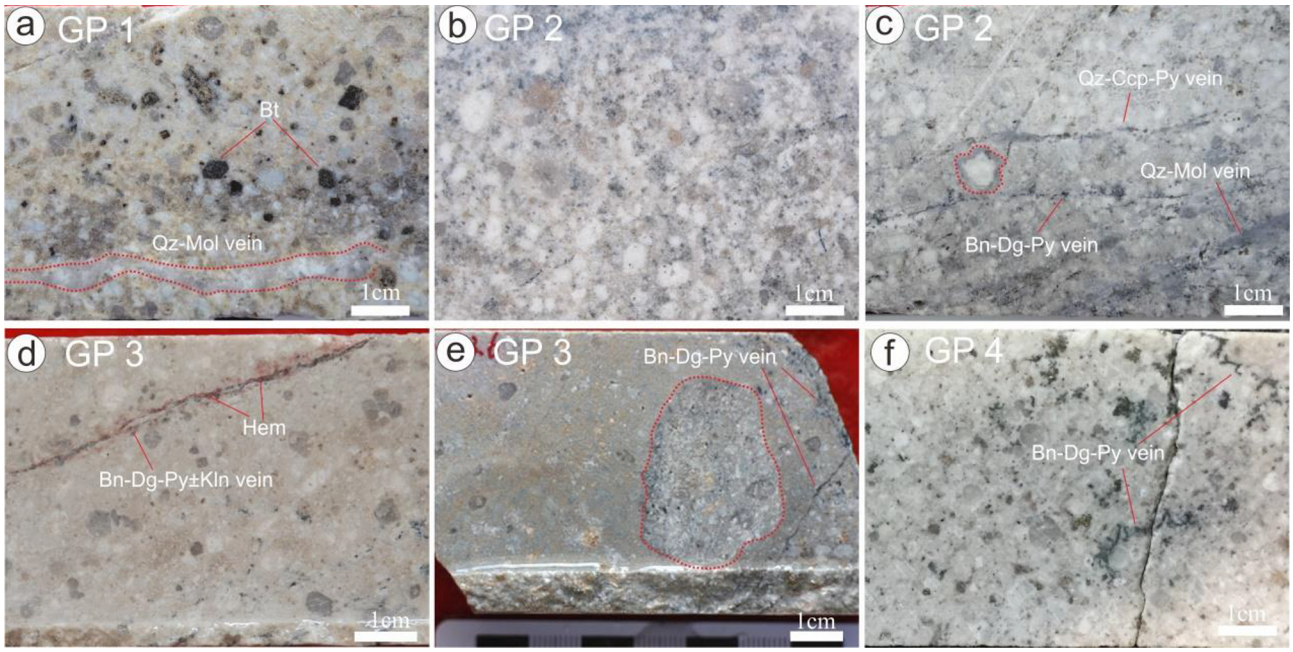

Fig. 4. Different phases of granodiorite porphyry intrusions. a, granodiorite porphyry 1 (GP 1), with biotite (Bt) phenocrysts and cut by quartz (Qz) – molybdenite (Mol) vein. b, granodiorite porphyry 2 (GP 2), containing more feldspar than quartz phenocrysts, strongly disseminated mineralized. c, granodiorite porphyry 2, with feldspar with grown of quartz cut by quartz-molybdenite vein, quartz-pyrite (Py) -chalcopyrite (Ccp) vein and bornite (Bn)- digenite (Dg)- pyrite vein. d, granodiorite porphyry 3 (GP 3), with quartz over feldspar phenocrysts, cut by a bornite-digenite-pyrite ± kaolinite (Kln) vein, with hematite (Hem) halo; e, granodiorite porphyry 3, cut by bornite-digenite-pyrite vein, trapped an enclave of earlier porphyry phase GP 2. f, granodiorite porphyry 4 (GP 4), consisting of a higher proportion of phenocrysts than GP 3, and more quartz phenocrysts than feldspar.

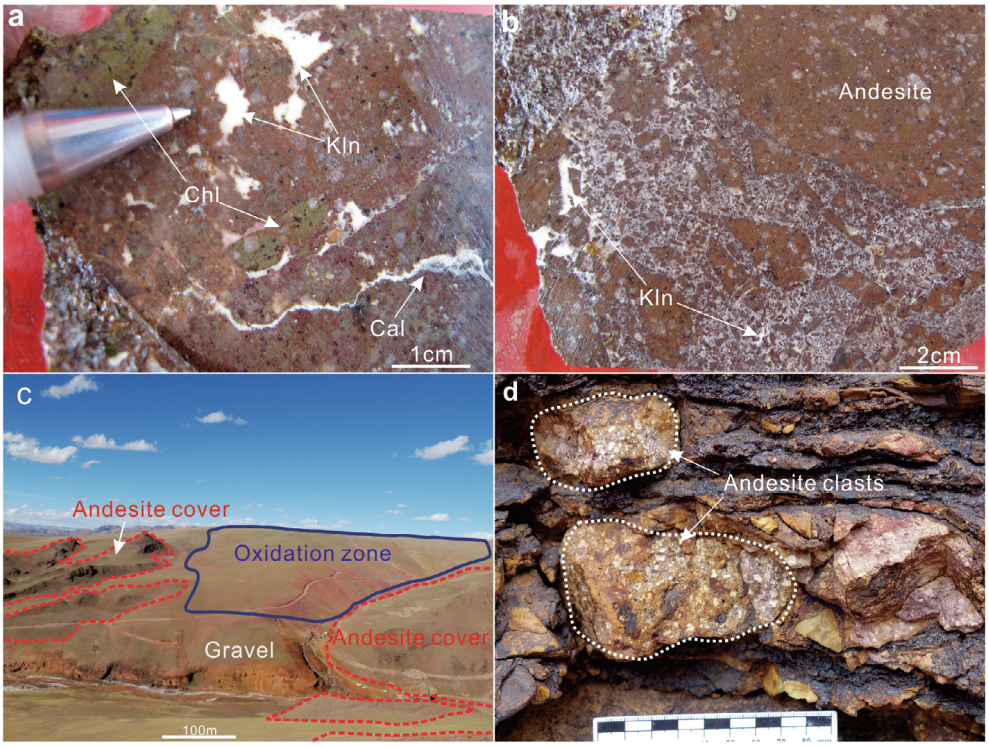

Fig. 5. Andesite and late conglomerate. a, weak propylitic alteration affected andesite with the occurrence of chlorite (Chl), calcite (Cal) vein and kaolinite (Kln) veins. b, Andesite hydrothermal breccia is cemented by kaolinite. c, Contact between andesite cover and gravel. d, Andesite clasts in the gravel.

chlorite ± pyrite veins are also present. D-type veins occur in the chlorite alteration zone, as well as minor A-type vein. Propylitic alteration is present in the andesite (Fig. 5a) in a small region at the southern part of the Tiegelongnan, but sulfide minerals are absent in the andesite.

6.4. Alunite alteration

Alunite alteration zone is characterized by multiple-stages of alunite-bearing veins and disseminated alunite and quartz (Table 2). Minor kaolinite, dickite, pyrophyllite, rutile, and barite occur in the alunite alteration zone. Early alunite I cements sericite-altered breccia with chalcopyrite-bornite-mineralized, and enargite and tennantite are hosted by this early alunite I (Fig. 8a). The alunite I breccia is cut by younger pyrite-enargite-tennantite veins and alunite II-sulfide veins (Fig. 8b). Laminated alunite II-sulfide veins (Fig. 8c) are widespread and are the main epithermal mineralization stage. Sulfides within the alunite II consist mainly of bornite, tennantite, and enargite, with minor chalcopyrite, and digenite, and show complex replacement texture (Table 2). The alunite II-sulfide veins are found cutting earlier D-type veins and pyrite veins (Fig. 8d), and also filling in D-type veins and pyrite veins. The complicated sulfides assemblages are also found filling D-type veins and pyrite veins without alunite. Alunite III veins fill earlier D-type quartz-pyrite veins, with minor disseminated enargite (Fig. 8e). Another stage of wide alunite IV-sulfide veins contains pyrite and trace amounts of enargite (Fig. 8f).

6.5. Kaolinite-dickite alteration

Kaolinite is the dominant mineral with minor dickite within the kaolinite-dickite alteration zone, where dickite occurs in the deep parts of the kaolinite-dickite alteration zone and closely relate to pyrophyllite in sericite alteration zone. Small amounts of alunite, illite, gypsum, diaspore, nackite, and goyazite occur in this alteration zone. Multiple stages of kaolinite veins and breccia are present in the kaolinite-dickite alteration zone. Barren white kaolinite is found cementing sericite-altered sandstone breccia. Compressive structures are shown in some kaolinite cemented breccia (Fig. 9a). These white kaolinite veins fill in earlier A-, B-, D-type veins, and alunite veins. These textures indicate a repeated opening of earlier formed veins and open-space filling by younger hydrothermal minerals. Few disseminated enargite and tennantite occur in these kaolinite veins. Barren kaolinite is found cement post-mineral andesite breccia (Fig. 5b). A lot of tennantite-enargite-containing dark and grey kaolinite veins are commonly present in this zone. Some of those veins fill the center of quartz veins to a depth of around 850 m (Fig. 9b), with the replacement of chalcopyrite by covellite and then by tennantite and enargite (Fig. 9c).

6.6. Sulfides and grade distribution

The sulfides in the Tiegelongnan deposit show vertical zonation (Fig. 10a and c). In deep parts of the sericite alteration and biotite hornfels, from around 1000 to 1200 m depth, molybdenite, chalcopyrite, and pyrite predominate in A- and B-type quartz veins (Fig. 10a). The disseminated chalcopyrite-bornite-pyrite assemblage characterizes the sericite alteration zone above 1000 m depth, which corresponds to a high Cu grade (> 0.8% Cu) zone associated with a relatively high Au (> 0.1 g/t) grade zone (Fig. 10b), and that represents the porphyry Cu mineralization center. The correlation between high Cu and Au grades suggests Au precipitated with Cu.

A telescoped zonation with high sulfidation minerals covellite, tennantite, and enargite is superimposed on bornite–chalcopyrite zone at the top of the sericite alteration zone (Fig. 10a and c). High Cu and Au grades characterize this zone (Fig. 10b and d).

In shallow parts of the Tiegelongnan deposit, high sulfidation minerals, including bornite, digenite, enargite, and tennantite are associated with the advanced argillic alteration zone, which is characterized by kaolinite-sulfide veins and alunite-sulfide veins. High grades of Cu (> 0.8% Cu) and > 0.1 g/t Au are common in these veins.

Supergene chalcocite veins at the top, and in the southern part of

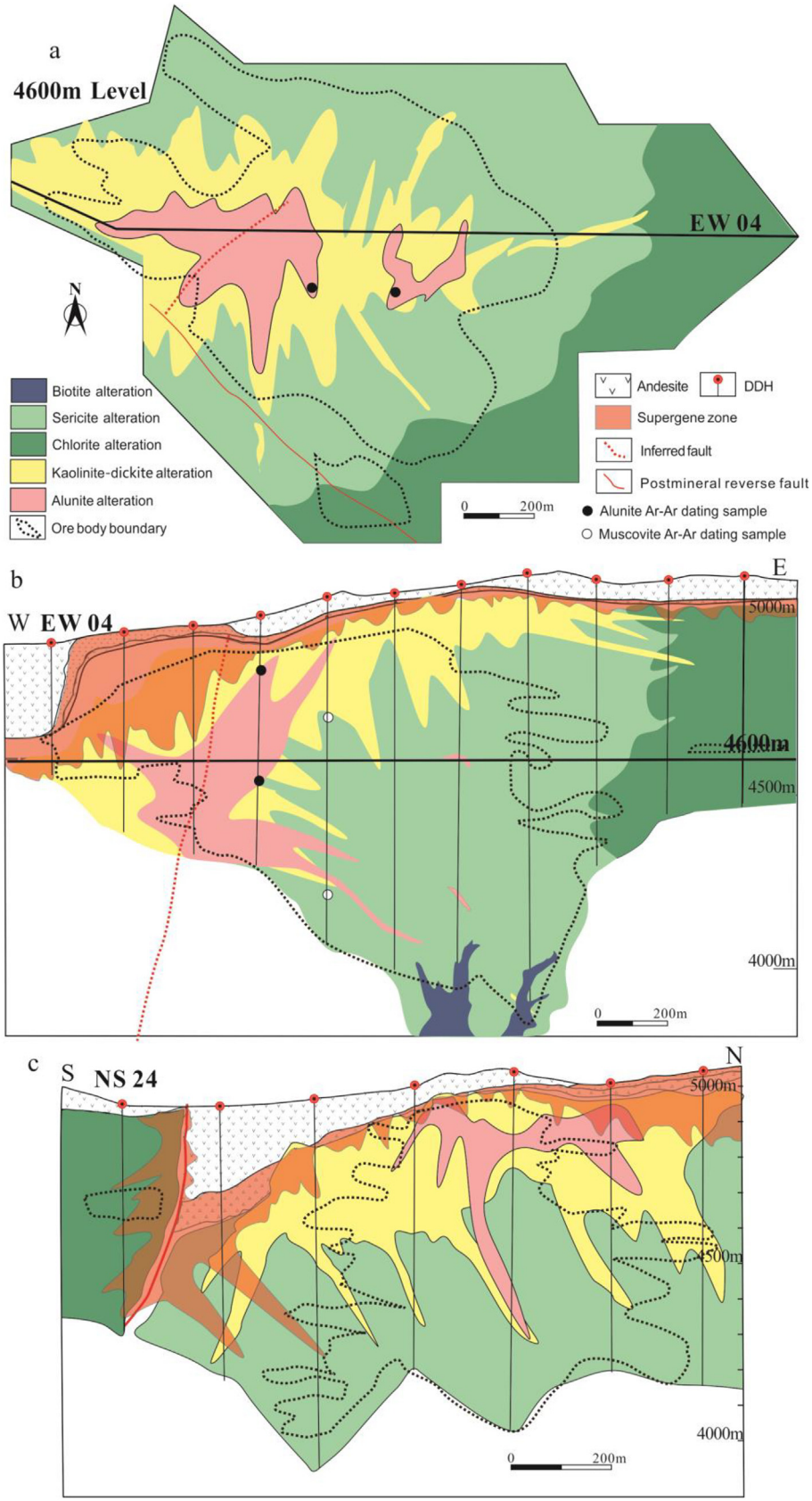

Fig. 6. Alteration distribution patterns of the 4600 elevation level (a), the cross-section EW 04 (b), and cross-section NS 24 (c) of the Tiegelongnan deposit.

Table 2
Characteristics of the Tiegelongnan deposit alteration and mineralization.

Hydrothermal episodes	Gangue minerals	Vein types	Sulfide mineral and texture	Textures description	Ar-Ar ages (Ma)
Supergene oxidation	Kln, Qz, Jar, Gth, Hem	Hem vein, Cc vein, Mal-Azu vein, Native Cu	Pyrite is replaced by chalcocite. Native gold is present at the shallow place, and native copper occurs in goethite veins	Goethite breccia is cemented by alunite-kaolinite. Pyrite in chlorite and quartz veins is oxidized to hematite. Kaolinite-sulfide veins, and alunite-sulfide veins are oxidized with the occurrence of hematite, malachite, and chalcocite.	
Kaolinite-dickite alteration	Kln and Dic assemblage with minor Alu, Dia, Ser, Nac, Goy	Kln vein Kln-Eng-Tnt vein	Tennantite and enargite occur in kaolinite veins and replace bornite and digenite	Kaolinite fills A-type, B-type, D-type quartz veins, and alunite veins. Kaolinite replaces biotite and sericite	
Alunite alteration	K-Alu and Qz assemblage with minor Na-Alu, Pyro, Mus, Kln Rut.	Multiple alunite veins including: Type-I: breccia cemented Alu-sulfide ± Kln vein Type-II: Laminated Alu ± Py ± Eng-Tnt ± bornite vein, Type-III: Alu vein fills Qz vein, Type-IV: wide Alu-Py vein	Tennantite and enargite are the main Cu-sulfides in alunite veins. Bornite occurs in alunite veins with minor chalcopyrite. Bornite-chalcopyrite-digenitee replaced by enargite and tennantite.	Alunite veins cut and fill D-type quartz veins, and alunite cement sericite alteration breccia.	Alu IV: 100.6 ± 2.0 Alu III: 112.5 ± 0.8 Alu II: 111.7 ± 1.0 Alu I: 116.3 ± 0.8
Chlorite alteration	Chl, Epi, Cal, Py assemblage	Chl-Py ± Ccp ± Qz ± Cal vein Cal vein Py-Cc vein	Pyrite occurs with minor chalcopyrite; Pyrite is replaced by chalcocite	Kaolinite veins cut chlorite-pyrite veins. Chalcocite replace pyrite, and some pyrite is oxidized to hematite	
Sericite alteration	Main Mus-Qz- Py assemblage, with the occurrence of minor Mag, Gps, Rut, Phen, Hem, Tour	Qz-Mol ± Ccp ± Py vein, Qz-Bn-Ccp-Py ± Gps vein Bn-Ccp massive vein Qz-Py ± Gps vein Py vein	Main sulfides including chalcopyrite, bornite, and pyrite occur with minor molybdenite, sphalerite, and galena. Chalcopyrite and bornite are replaced by covellite, digenite, enargite, and tennantite.	Kaolinite fills Quartz veins. Muscovite is replaced by Kaolinite, dickite, and pyrophyllite in the shallow parts. Some pyrites are replaced by Cu-sulfides	120.9 ± 0.8 108.7 ± 0.7
Biotite alteration	Bt	Barren Qz vein Qz-Ccp-Py vein Qz-Bt-Mol ± Ccp ± Py vein Bio-Ccp vein	Chalcopyrite occurs with molybdenite and pyrite	Biotite veins mostly replaced by sericite and kaolinite	121.1 ± 0.6[1]

Abbreviations: Alu-alunite, Azu-azurite, Bn-bornite, Bt-biotite, Cal-calcite, Cc-chalcocite, Ccp-chalcopyrite, Cv-covellite, Dg-digenite, Dia-diaspore, Dic-dickite, Eng-enargite, Goy–goyazite, Gps-gupsum, Gth-goethite, Hem-hematite, Ill-illite, Kln-kaolinite, Mag-magnetite, Mal-Malachite, Mol-molybdenite, Nac-nacrite, Phen-phengite, Py-pyrite, Pyro-pyrophyllite, Qz-quartz, Rut-rutile, Tnt-tennantite, Tour-tourmaline.
1 – data from Lin et al., 2017a.

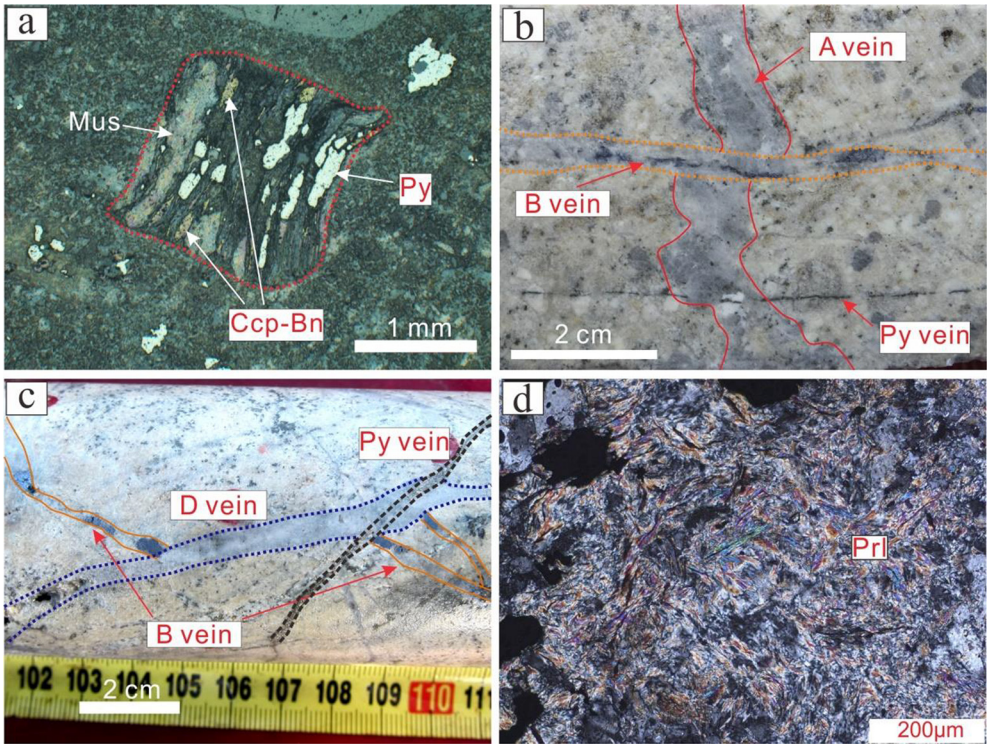

Fig. 7. Alteration and cross-cutting veins in the sericite and transition alteration zone. a, Plagioclase phenocrysts are altered to muscovite (Mus) with chalcopyrite (Ccp), bornite (Bn) mineralization. b, Sericite altered granodiorite porphyry 1 is cut by A-type quartz-chalcopyrite ± bornite vein, which is cut by B type quartz (Qz)-molybdenite (Mol) vein and pyrite (Py) vein. c, Sericite altered sandstone is cut by B-type vein, which is cut by D-type quartz-pyrite vein and then by pyrite vein. d, Pyrophyllite (Prl) alteration.

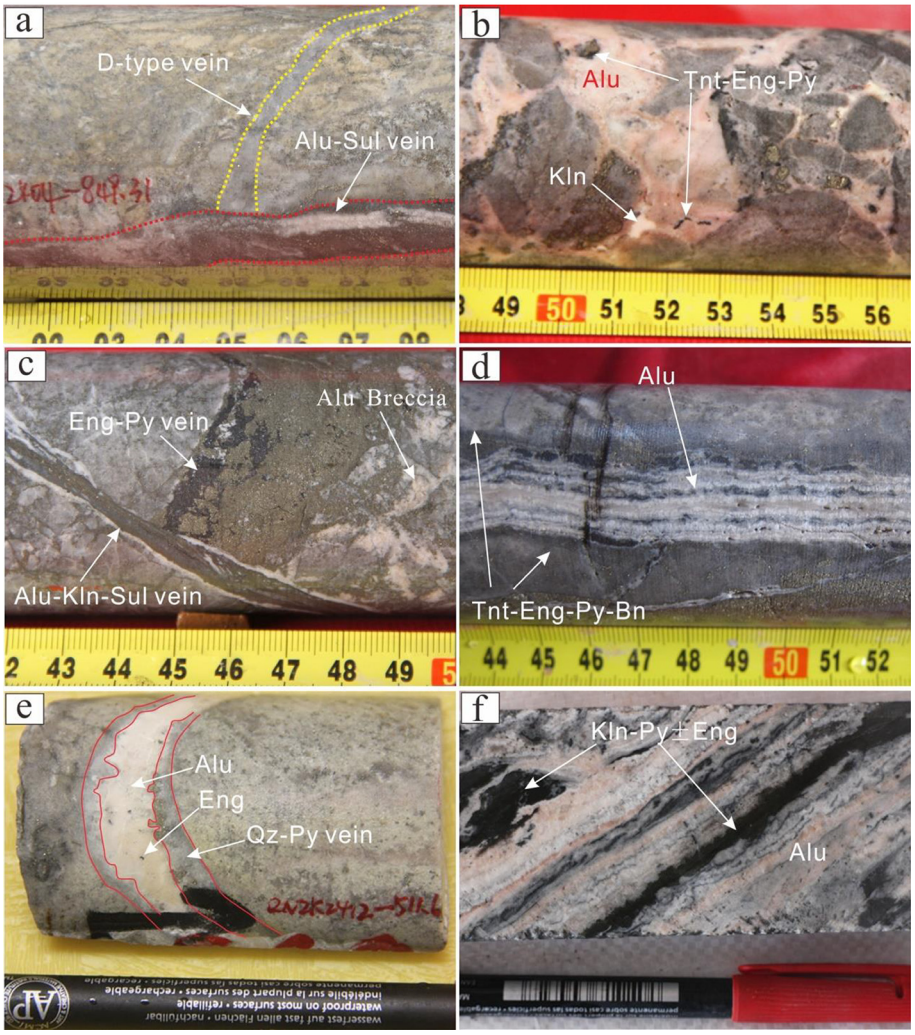

Fig. 8. Alunite veins feature and alunite samples for ^{40}Ar-^{39}Ar dating. a, alunite (Alu) -sulfide (Sul) vein cuts sericite alteration rock and quartz (Qz) -chalcopyrite (Ccp) -pyrite (Py) vein. b, Sample 1604-429 (alunite I) for dating, alunite, and tennantite (Tnt) -enargite (Eng) cemented sericite alteration wall rocks breccia, and with late kaolinite (Kln) filling. c, Pure alunite breccia is cut by enargite-pyrite vein, which is then cut by younger kaolinite-alunite-sulfide vein. d, Sample 1604-171 (alunite II) for dating, laminated alunite-sulfide veins, sulfides mainly including tennantite, enargite, pyrite, and bornite (bn). e, Sample 2412-511 (alunite III) for dating, alunite fills in quartz-pyrite veins with disseminated enargite inside. f, Sample 3212-206 (alunite IV) for dating, laminated alunite veins containing kaolinite-pyrite and a trace amount of enargite.

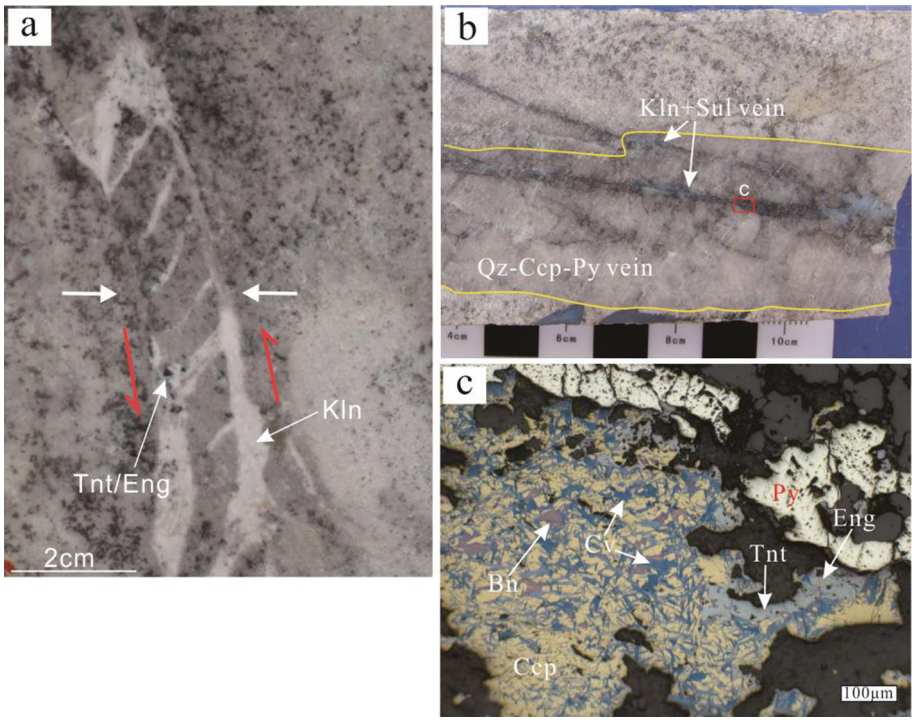

Fig. 9. Vein filling and cut texture and superposition of high sulfidation assemblages. a, Compressive breccia is cemented by kaolinite and tennantite/enargite. b, kaolinite (Kln)-sulfide (Sul) veins cut and fill in early quartz (Qz)-chalcopyrite (Ccp)-pyrite (Py) vein. c, chalcopyrite, and bornite (Bn) are replaced by covellite (Cv), and then replaced by tennantite and enargite.

the Tiegelongnan deposit (Fig. 10a and c) are characterized by a high grade of Cu (> 0.8%), as a result of supergene enrichment (Fig. 10b and d). However, the Au grade is low (< 0.1 g/t) in the supergene zone (Fig. 10d).

6.7. Supergene zone

The major part of the erosional breccia, with a thickness of few to tens of meters, is affected by supergene oxidation beneath (Fig. 6b and

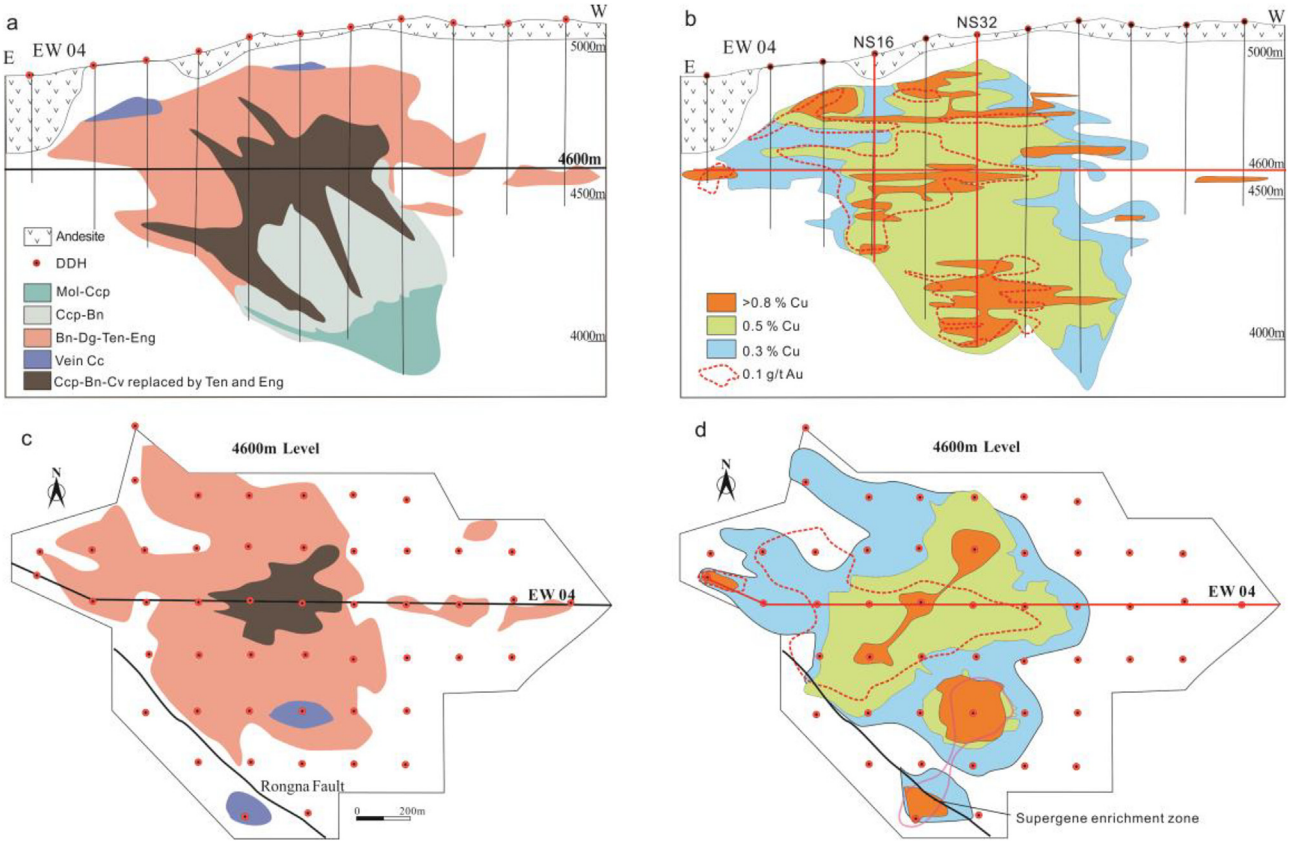

Fig. 10. Sulfide assemblage distribution at the 4600 m elevation level (a), and the Line 04 cross-section (c), Cu and Au grade distribution at 4600 m elevation level (b), and the Line 04 cross-section (d), Rongna Fault is the post-cover reverse fault. Bn-bornite, Cc-chalcocite, Ccp-chalcopyrite, Cv-covellite, Dg-digenite, Eng-enargite, Mol-molybdenite, Tnt-tennantite.

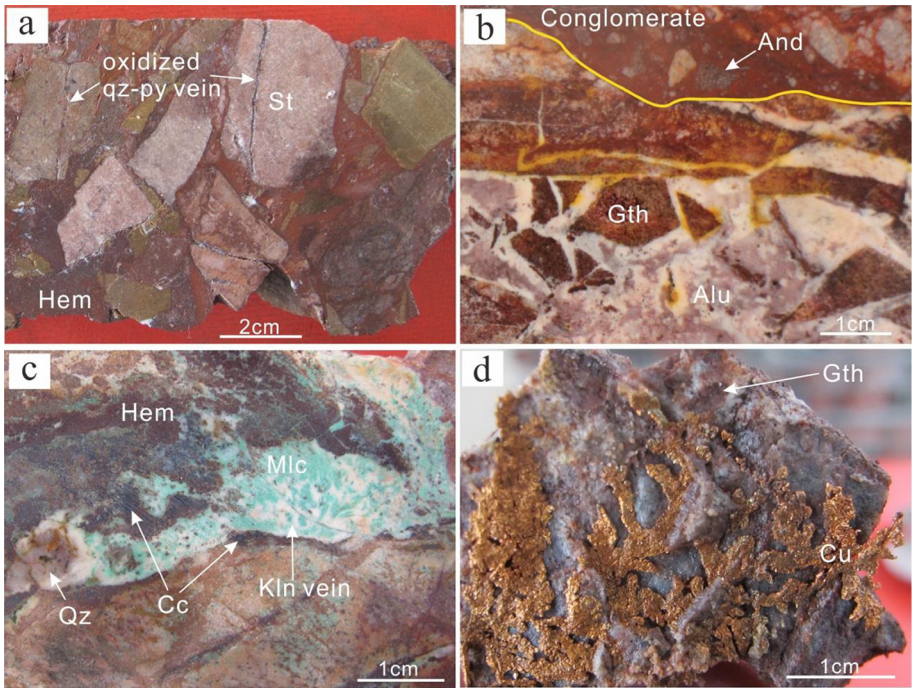

Fig. 11. Erosional breccia and supergene oxidization at the top of the Tiegelongnan deposit. a, Breccia (sandstone (St), containing oxidized quartz (Qz) – pyrite (Py) vein) is oxidized and cemented by hematite (Hem). b, Goethite (Gth) breccia is cemented by I-type alunite (Alu), which is covered with andesite (And)-contain conglomerate. c, Sulfide in kaolinite veins is oxidized to hematite and malachite (Mlc), with supergene enrichment of chalcocite (Cc). d, Native copper (Cu) and goethite are present in the fracture of oxidized rocks.

c). The supergene zone is hundreds of meters thick at places where andesite is eroded or cut by the post-andesite fault (Fig. 6b, c), where it reaches a depth of ~600 m in the southern part of Tiegelongnan. In the breccia, some of the rounded and angular clasts are cemented by hematite (Fig. 11a). Sulfides in quartz veins (A and D-type vein) in the erosional breccia are oxidized to hematite (Fig. 11a). Jarosite and goethite are dominant at shallow cuttings, where some native gold is found. Alunite I cements goethite breccia (Fig. 11b), which suggests the supergene event started before this epithermal activity. Part of the advanced argillic alteration zone is affected by supergene oxidation, which resulted in sulfides oxidized to hematite, azurite, and malachite in kaolinite veins, with the formation of supergene chalcocite (Fig. 11c). A minor amount of native copper is present in this supergene oxidizing zone (Fig. 11d).

7. Methodology

7.1. Samples selected for dating

Drill core samples for zircon U-Pb dating were collected from granodiorite porphyry phases 3 and 4. Samples 2404a and 2404b are from GP 3 (Fig. 3) for high precision CA-ID-TIMS dating. Samples 2404-450 and 2405-598 for LA-ICP-MS zircon U-Pb dating are from mineralized GP 4, which are collected from the middle and western parts of the Tieglongnan deposit, located at depth of ~450–600 m depth (Fig. 3).

Hydrothermal muscovite and alunite were carefully separated from altered granodiorite porphyries, breccias and veins samples for ^{40}Ar-^{39}Ar dating. Hydrothermal muscovite was picked from a sample of GP 2 (2404-737) and a sample of GP 3 (2404-313). Alunite was separated from alunite-kaolinite-sulfides breccia (1604-429, alunite I), laminated alunite-sulfide veins (1604-171, alunite II), quartz-alunite-sulfide veins (2412-511, alunite III) and massive and laminated alunite ± kaolinite-sulfides veins (3212-206, alunite IV) (Fig. 8).

7.2. Analytical methods

CA-ID-TIMS zircon U-Pb dating was carried at the Pacific Centre for Isotopic and Geochemical Research (UBC), using methods described in (Scoates and Friedman, 2008). LA-ICP-MS zircon U-Pb dating was carried at the Tianjin Institute of Geology and Mineral Resources, following the method of (Geng et al., 2012). ^{40}Ar-^{39}Ar geochronology of muscovite sample 2404-737 and alunite breccia sample 1604-429 were carried in the Testing Center of Nuclear Industry Geology Research Institute of Beijing, following the method described in (Lin et al., 2017a); ^{40}Ar-^{39}Ar ages of muscovite sample 2404-313, and that of alunite samples 1604-171, 2412-511, and 3212-206 was acquired at the Pacific Centre for Isotopic and Geochemical Research, (UBC), following (Madrid et al., 2017). All analytical methods and data are provided in detail in the Supplementary data.

8. Results

High-resolution CA-ID-TIMS isochron ages for two samples of GP 3 are shown in Fig. 12 and Supp. Table 1A. The weighted mean ^{206}Pb/^{238}U age of the two grains from sample 2404a is 119.9 ± 0.1 Ma (Fig. 12a). Three zircon grains were analyzed from sample 2404b: two grains give a weighted mean age of 119.7 ± 0.2 Ma, whereas the third grain yields an younger age of 119.1 ± 0.2 Ma (Fig. 12b). Two grains from sample 2404a and the two grains with an age 119.7 ± 0.2 Ma from sample 2404b give a mean age of 119.9 ± 0.2 Ma (Fig. 12c).

Sample 2405-598 yields a weighted mean age of 116.5 ± 0.7 Ma, whereas sample 2404-450 gave an age of 115.9 ± 0.4 Ma, (Fig. 13 and Supp. Table 2A). The two ages are within the 2σ error, such that a mean age of 116.2 ± 0.4 Ma is computed.

Hypogene alteration muscovite and alunite ^{40}Ar-^{39}Ar age spectra, and inverse isochron plots are presented in Fig. 14 and Supp. Table 3A. Muscovite sample 2404-757 from GP 2 yields a plateau age of 120.9 ± 0.8 Ma for 99.82% ^{39}Ar release, and an inverse isochron age of 122.0 ± 0.9 Ma. A low ^{40}Ar-^{36}Ar$_i$ value 229.0 ± 2.7 (less than that of atmosphere 295) suggests slight Ar loss for this sample. The muscovite sample 2404-313 from GP 3 yields a plateau age of 108.7 ± 0.7 Ma, with 92.2% ^{39}Ar released, and inverse isochron age of 107.7 ± 0.7 Ma.

Alunite I (1604-429) gives a flat plateau age of 116.3 ± 0.8 Ma, with 81.4% ^{39}Ar released (Fig. 14). Its inverse isochron age is 115.5 ± 1.6 Ma with a high ^{40}Ar-^{36}Ar$_i$ value 343.5 ± 79.9 (> 295) (Fig. 14), which may suggest extraneous argon. Alunite II (1604-171)

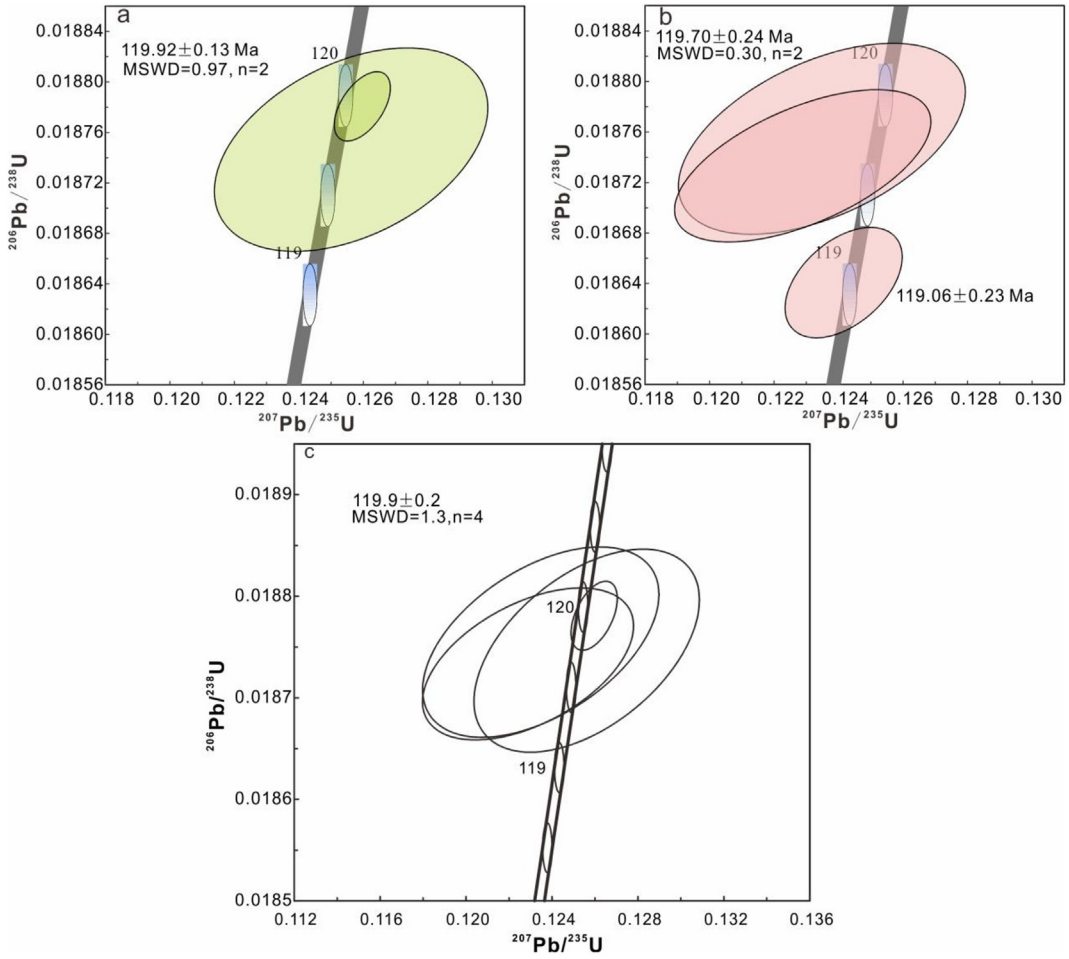

Fig. 12. Concordia plots of CA-ID-TIMS zircon ^{206}U-^{238}Pb dating of granodiorite porphyry 3, sample 2404a (a), sample 2404b (b), and a combination of the four consistent data (c).

from laminated alunite-sulfides vein yields a total-gas age of 111.7 ± 1.0 Ma (Fig. 14), and an inverse isochron age of 110.5 ± 2.1 Ma. Alunite III (2412-511) from an alunite-quartz vein gives an almost flat total-gas age of 112.5 ± 0.8 Ma, with 99.95% ^{39}Ar release, and an inverse isochron age of 110.5 ± 2.1 Ma (Fig. 14). Alunite IV (3212-206) from a wide alunite-sulfides vein has a younger plateau age of 100.6 ± 2.0 Ma with 96.5% ^{39}Ar release, and an inverse isochron age of 99.1 ± 2.3 Ma (Fig. 14).

9. Discussion

9.1. Geochronology of the Tiegelongnan deposit

Geochronological data demonstrate that the Tiegelongnan deposit formed by a series of magmatic and hydrothermal events (Table 3 and Fig. 15). Lin et al. (2017b) dated the diorite porphyry at 123.1 ± 1.7 Ma, which is the oldest magmatic event in the Tiegelongnan deposit. The GP 1 porphyry is dated at 121.5 ± 1.5 Ma

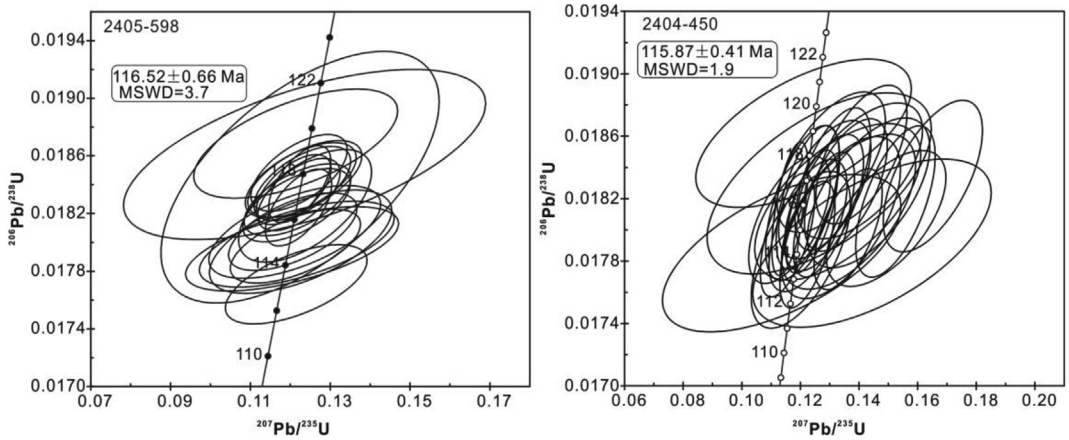

Fig. 13. Concordia plots of LA-ICP-MS zircon ^{206}U-^{238} Pb dating of granodiorite porphyry 4, Sample 2405-598 and 2404-450.

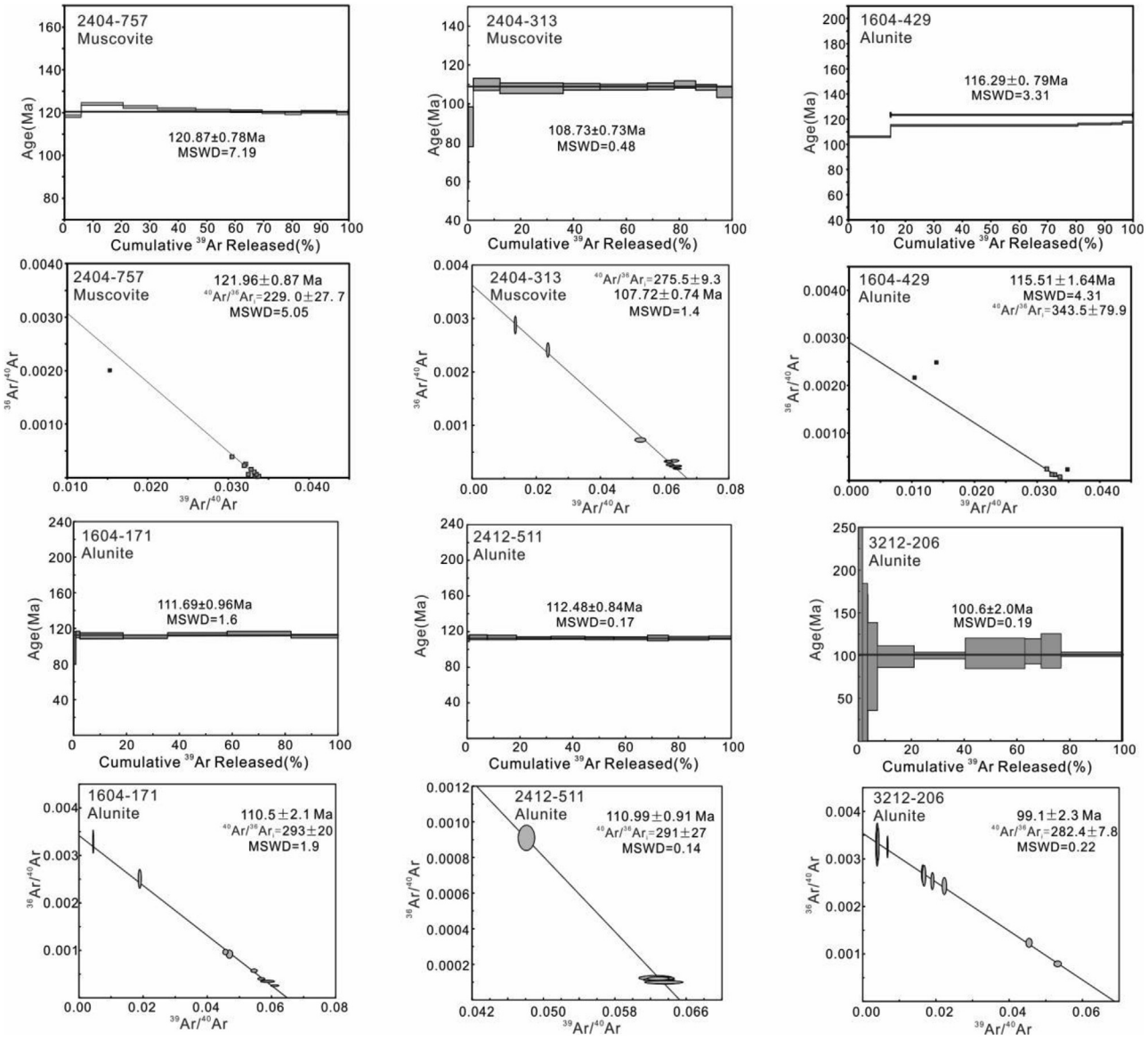

Fig. 14. Muscovite and alunite ^{40}Ar-^{39}Ar age spectra from the Tiegelongnan deposit. For each sample, two graphs show plateau spectrum age, and corresponding inverse isochron age.

(zircon LA-ICP-MS age; Lin et al., 2017b). Fang et al. (2015) documented the strongly mineralized GP 2 porphyry with an age of 120.2 ± 1.0 Ma (zircon LA-ICP-MS age), which is consistent with molybdenite Re-Os ages of 121.2 ± 0.6 Ma (Lin et al., 2017b) and 119.0 ± 1.4 Ma (Fang et al., 2015). Another GP 2 was dated with an age of 118.7 ± 0.9 Ma (Zhang et al., 2018), which is slightly younger but within the error of the LA-ICP-MS age of 120.2 ± 1.0 Ma. One hydrothermal biotite has a ^{40}Ar-^{39}Ar age of 121.1 ± 0.6 Ma (Lin et al., 2017a), which is consistent with the ages of GP 1, GP 2, and molybdenite, within the uncertainty. Muscovite 2404-737 from GP 2 with an age of 120.9 ± 0.8 Ma is consistent with the GP 2 porphyry age of 120.2 ± 1.0 Ma. High-precision CA-ID-TIMS ages of GP 3 intrusions are 119.9 ± 0.2 (n = 4) and 119.1 ± 0.2 Ma (n = 1). The age of 119.9 ± 0.2 Ma is consistent with ages of hydrothermal biotite and muscovite, although the GP3 is strongly affected by advanced argillic alteration. The younger GP3 age of 119.1 ± 0.2 Ma does not overlap within error with 119.9 ± 0.2 Ma, suggesting perhaps a slightly younger intrusive dike identified as GP3, misclassified because of strong overprinting by hydrothermal alteration. Minor Pb loss, however, can not be ruled out, which could cause a slightly younger age. Muscovite, biotite, and molybdenite hosted by GP1 and GP 2 intrusions and their adjacent wallrock sandstone are all overlapping in age between ~121 and ~119 Ma (Fig. 15). The high-precision CA-ID-TIMS age of 119.9 ± 0.2 Ma is proposed to represent the precise age of porphyry hydrothermal event.

The GP 4 porphyry has a mean age of 116.2 ± 0.4 Ma, which is about 3 Ma younger than the porphyry stage alteration and mineralization. One feldspar porphyry sample (RN2404-300) was dated at 117.1 ± 0.9 Ma (Zhang et al., 2018), which is consistent with the ages for GP 4. Alunite from one laminated alunite-sulfide vein yields ^{40}Ar-^{39}Ar age of 117.9 ± 1.6 Ma, whereas pyrite from this vein has Rb-Sr age of 117.5 ± 1.8 Ma (Lin et al., 2017a), which overlapped the alunite I age of 116.3 ± 0.8 Ma obtained from this study. The ages of alunite I and the alunite sample in Lin et al., (2017a) are consistent with the GP 4 age of 116.2 ± 0.4 Ma, and feldspar porphyry age 117.1 ± 0.9 Ma, suggesting that they may result from the same magmatic-hydrothermal event. The ~116 Ma alunite I age is older than the alunite II age of 111.7 ± 1.0 Ma, which is consistent with laminated veins cutting alunite breccia (Fig. 9c). Alunite III, with an age of 112.5 ± 0.8 Ma, is within the error of the age of alunite II. The alunite

Table 3
Summary of samples and results of geochronology at the Tiegelongnan deposit, Tibet.

Stage	Sample No.	Samples	Dating mineral	Method	Age (Ma)	Samples Description	References
Porphyry stages	ZK3228-507	Diorite porphyry	Zircon	LA-ICP-MS	123.1 ± 1.7	Affected by chlorite alteration with the occurrence of some chlorite-pyrite vein	Lin et al., 2017b
	ZK4804-1259	Granodiorite porphyry 1	Zircon	LA-ICP-MS	121.5 ± 1.5	Biotite-bearing granodiorite porphyry 1, with sericite alteration, no quartz vein	Lin et al., 2017b
	ZK1612-373	Granodiorite porphyry 2	Zircon	LA-ICP-MS	120.2 ± 1.0	Sericite alteration granodiorite porphyry 2, without quartz vein	Fang et al., 2015
	RN2404-777	Granodiorite porphyry 2	Zircon	SIMS	118.7 ± 0.9	Sericite alteration and ore-bearing porphyry	Zhang et al., 2018
	2404a	Granodiorite porphyry 3	Zircon	CA-ID-TIMS	119.9 ± 0.1	Sericite alteration porphyry dike, with digenite-bornite veins.	This study
	2404b	Granodiorite porphyry 3	Zircon	CA-ID-TIMS	119.7 ± 0.2 119.1 ± 0.2	Sericite alteration porphyry dike, with digenite-bornite veins.	This study
	Mol-01	Qtz-Mol veins	Molybdenite	Re-Os	121.2 ± 0.6	Quartz-Molybdenite veins	Lin et al., 2017b
	Mol-02	Qtz-Mol veins	Molybdenite	Re-Os	119.0 ± 1.4	Quartz-Molybdenite veins	Fang et al., 2015
	ZK4804-1222	Qtz-Mol-Ccp-Bio vein	Biotite	^{40}Ar-^{39}Ar	121.1 ± 0.6	Quartz-molybdenite-chalcopyrite-biotite vein	Lin et al., 2017a
	ZK2404-737	Granodiorite porphyry 2	Muscovite	^{40}Ar-^{39}Ar	120.9 ± 0.8	Muscovite separated from GP 2	This study
Epithermal stages	2405-598	Granodiorite porphyry 4	Zircon	LA-ICP-MS U-Pb	116.5 ± 0.7	Sericite alteration and dickite-pyrophyllite alteration porphyry dike, with disseminated digenite, covellite, enargite.	This study
	2404-450	Granodiorite porphyry 4	Zircon	LA-ICP-MS U-Pb	115.9 ± 0.4	Sericite alteration and dickite-pyrophyllite alteration porphyry dike, with disseminated digenite, covellite, enargite.	This study
	RN2404-300	feldspar porphyry	Zircon	SIMS	117.1 ± 0.9	Argillic alteration	Zhang et al., 2018
	ZK1604-383	Alunite-sulfides veins	Alunite	^{40}Ar-^{39}Ar	117.9 ± 1.6	Wide laminated alunite-pyrite-enargite veins, with few kaolinite and dickite	Lin et al., 2017a
	PY-1	Alunite-sulfides veins	Pyrite	Rb-Sr	117.5 ± 1.8	Wide laminated alunite-pyrite-enargite veins, with few kaolinite and dickite	Lin et al., 2017a
	1604-429	Alunite breccia (alunite I)	Alunite	^{40}Ar-^{39}Ar	116.3 ± 0.8	Alunite (with enargite-tennantite-digenite) cement sericite-altered wall rocks	This study
	1604-171	Alunite-sulfides vein (alunite II)	Alunite	^{40}Ar-^{39}Ar	111.7 ± 1.0	Narrow laminated alunite-sulfide veins, with kaolinite	This study
	2412-511	Alunite-quartz vein (alunite III)	Alunite	^{40}Ar-^{39}Ar	112.5 ± 0.8	Alunite fills quartz-pyrite vein	This study
	3212-206	Alunite-sulfides vein (alunite IV)	Alunite	^{40}Ar-^{39}Ar	100.6 ± 2.0	Wide laminated alunite-pyrite vein	This study
	2404-313	Granodiorite porphyry 3	Muscovite	^{40}Ar-^{39}Ar	108.7 ± 0.7	Muscovite separated from GP 3	This study
Post-mineral	3220-66	Andesite	Zircon	LA-ICP-MS U-Pb	111.7 ± 1.6	Non-alteration fresh andesite at the top of the mineralized sandstone	Lin et al., 2017b
	RN-GS01	Andesite	Zircon	LA-ICP-MS U-Pb	110.1 ± 0.7	Non-alteration fresh andesite at the top of the mineralized sandstone	Wang et al., 2015

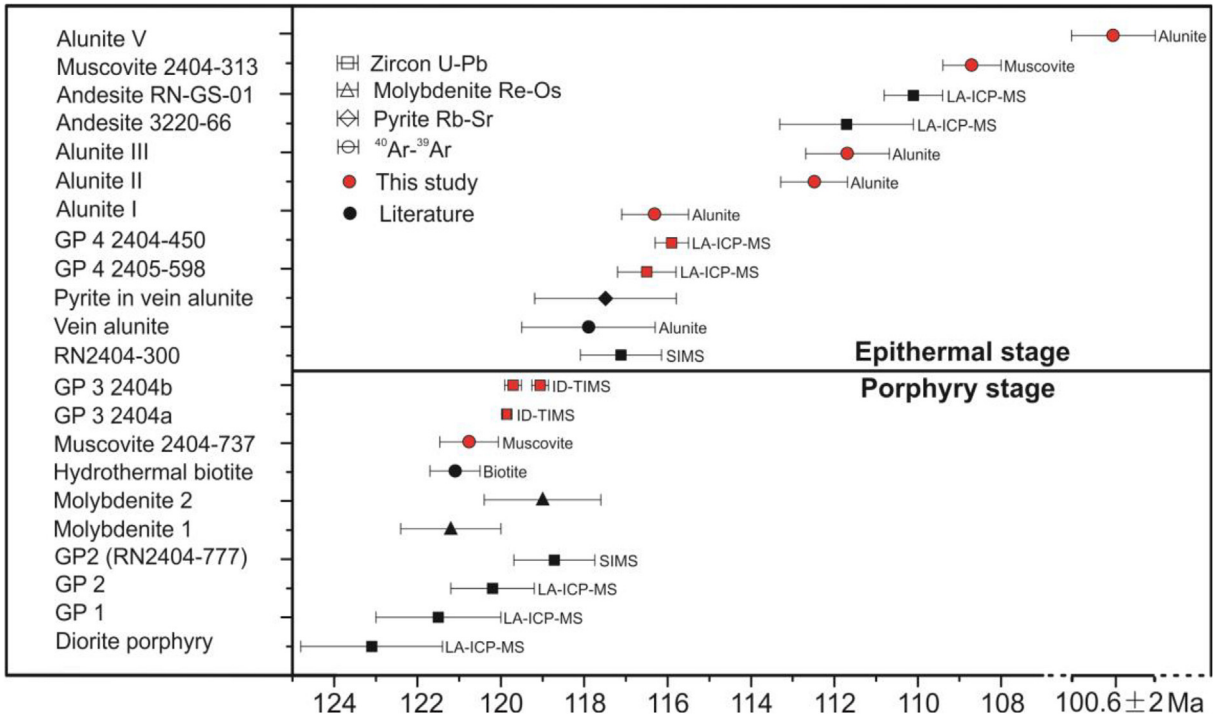

Fig. 15. Geochronological data for the Tiegelongnan deposit, with comparison to literature. GP1, molybdenite 1, and andesite 3220-66 ages from Lin et al. (2017b); GP2 and molybdenite 2 ages from Fang et al. (2015); hydrothermal biotite, vein alunite age from Lin et al. (2017a); andesite RN-GS-01 age from Wang et al. (2015); SIMS zircon data from Zhang et al. (2018).

V is younger with an age of 100.6 ± 2.0 Ma.

The andesite cover is dated at 110.1 ± 0.7 Ma (zircon LA-ICP-MS age; Wang et al., 2015), and 111.7 ± 1.6 Ma (zircon LA-ICP-MS age; Lin et al., 2017b). These ages are close to the ages of alunite II and alunite III. However, the alunite II age is not overlapping within the error of the younger andesite age of 110.1 ± 0.7 Ma. The andesite cover is mostly unaltered and not mineralized, which is in contrast to the intense advanced argillic alteration and high sulfidation mineralization in the shallow parts of the deposit. Thus, andesite likely forms slightly younger than formation of alunite II and III.

Muscovite 2404-313 separated from the GP 3 gives a young age of 108.7 ± 0.7 Ma, which is much younger than the GP 3 CA-ID-TIMS ages between 119.9 ± 0.2 Ma, but consistent with ages of andesite. Muscovite ^{40}Ar-^{39}Ar ages are vulnerable to thermal events because of its low closure temperature (300–400 °C; Chiaradia et al., 2013). The andesite emplaced at 110.1 ± 0.7 Ma is possible to cause the reset of this muscovite age, considering the muscovite age is close to the andesite ages. However, the flat plateau spectra of the sample muscovite 2404-313 do not show stepping resetting features (Fig. 14). Its spatially nearby alunite samples from this study (Fig. 6) were not reset by younger hydrothermal events. Additionally, andesite is affected by weak hydrothermal alteration (Fig. 5a and b), which suggests hydrothermal activity is active after the eruption of andesite. So, the 108.7 ± 0.7 Ma age is interpreted to be linked with a young stage of hydrothermal activity, which may be associated with the formation of andesite.

The late alunite IV age (100.6 ± 2.0 Ma) is much younger than any other stage of intrusion or hydrothermal mineral. This very young alunite ^{40}Ar-^{39}Ar age may relate to a late magmatic activity.

9.2. Evolution of the Tiegelongnan deposit

Tiegelongnan displays several pulses of epithermal alteration and copper mineralization telescoping porphyry copper-molybdenum alteration and mineralization. Although the location and character of the NE-striking fault are not precisely understood, it is considered to control the formation of Tiegelongnan porphyry mineralization at ~120 Ma (Fig. 16a), as well as several other deposits in the Duolong district (Fig. 1; Song et al., 2018).

Exhumation associated with paleosurface declining had started before the first epithermal type advanced argillic alteration and high sulfidation mineralization at ~116 Ma (Fig. 16b). In term of regional tectonic, this ages corresponds to the early Cretaceous compressive tectonism in the continental arc of the Southern Qiangtang region, as a result of subduction of Bangong-Nujiang ocean (Li et al., 2016b; Li et al., 2019), or collision between Lhasa and Qiangtang terranes (Liu et al., 2015; Liu et al., 2017). As a result, Tiegelongnan underwent uplift and erosion, which is evidenced by muscovite and kaolinite replacing biotite, and advanced argillic alteration telescoping sericite and chlorite alteration. The overprinting situations are widely recognized in porphyry systems worldwide, and considered as results of paleosurface and water-table declining (Sillitoe, 1999; Sillitoe et al., 2019).

Younger stage of epithermal ores and advanced argillic alteration started at ~112 Ma (Fig. 16c). It likely formed under a similar environment to that of the first epithermal event. The erosion degree during the interval between the two epithermal events is difficult to assess. Fluid inclusion pressure calculation estimates around 1200 m of the deposit have been removed after 120 Ma, and around 500 m was removed after the formation of low-temperature quartz veins from advanced argillic alteration zone (Yang et al., 2014). If the calculation is reliable, around 700 m of erosional removal at Tiegelongnan likely happened between early (~120 Ma) and late magmatic-hydrothermal activities, although the age of later quartz vein is undetermined. Erosion may have continued after the second epithermal event and unroof the top of the epithermal system, because of lack of silicic cap at the top of Tiegelongnan, which is commonly found on top of porphyry Cu systems (Sillitoe, 2010).

The erosion of Tiegelongnan paused during the cover of andesite at ~110 Ma, which is associated with mild hydrothermal alteration without mineralization (Fig. 16d). The start of the supergene oxidation

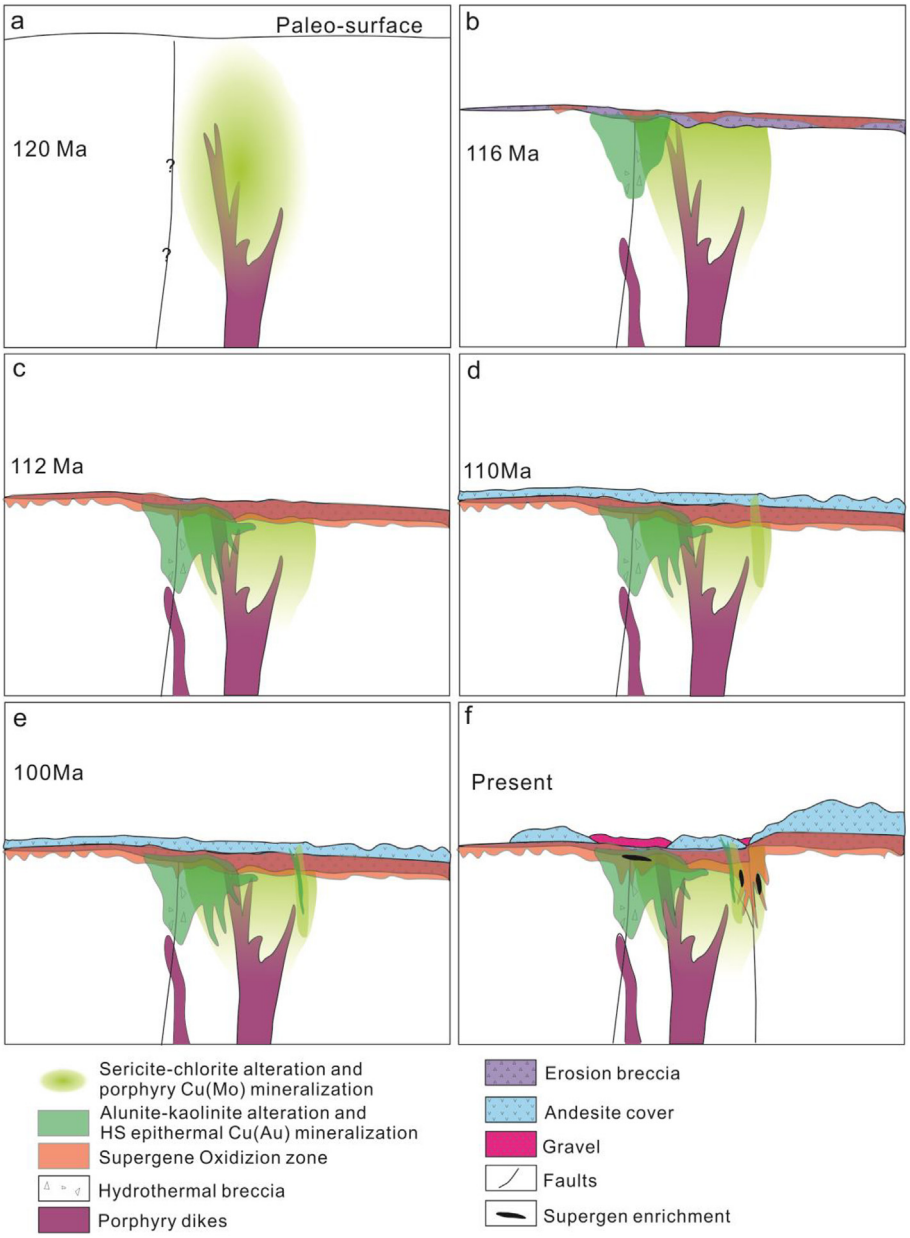

Fig. 16. Formation scheme for the Tiegelongnan deposit. a, Porphyry stage mineralization and alteration formed with intrusion several phases of granodiorite porphyries at ~120 Ma. b, The porphyry system is unroofed, and affected by erosion and supergene oxidation on the top. The first pulse of high-sulfidation epithermal hydrothermal event took place at ~116 Ma. c, A younger pulse of epithermal event induced at ~112 Ma, with continuing weathering, paleo-surface declining, and erosion. d, Andesite covered at the top of this porphyry-epithermal system at ~110 Ma, and it preserves the deposit from erosion, with weak hydrothermal alteration without sulfide mineralization. e, The youngest magmatic event happened with the formation of alunite at ~100 Ma. f, Andesite is partly eroded with the formation of supergene enrichment until the present.

event is unknown, but it should be earlier than the first epithermal event, as shown by goethite breccia cemented by barren kaolinite-alunite I (Fig. 11b).

The andesite cover was subsequently affected by weak hydrothermal alteration at ~100 Ma (Fig. 16e) without sulfide mineralization. The post-andesite thrust fault contributes to declining of groundwater from the southern part of Tiegelongnan.

After that, uplift and erosion of the Tibetan plateau resulted in the exposure of the Tiegelongnan deposit, more profound supergene oxidation with the formation of supergene enrichment (Fig. 16f). However, most parts of the Tiegelongnan deposit were protected by the andesite cover, which most like explain its preservation.

Exhumation of some porphyry deposits exceeding 1000 m and post-mineral cover usually takes place in a short time of less than ~2 m.y., such as the Oyu Tolgoi, Mongolia (Wainwright et al., 2017), Boyongan and Bayugo, Philippines (Braxton et al., 2018), and the Josemaría, Argentina (Sillitoe et al., 2019). Around 10 m.y. exhumation after the porphyry mineralization at Tiegelongnan is a slow and long exhumation process compared to those deposits. It is estimated at an exhumation rate of between 0.1 and 0.2 km / m.y. at the Tiegelongnan (Song et al., 2017). Climate is considered a robust control to the exhumation rate, with humid tropical regions characterized by a faster exhumation rate than dry regions (Yanites and Kesler, 2015). This is used to explain the rapid exhumation in the tropical Philippines and possibly low-latitudinal Mongolia conditions. However, a compressive uplift pulse during a specific period of time at the Andes is considered as a possible reason for the rapid exhumation at the semiarid Andean region (Sillitoe et al., 2019). North-western Tibet is a cold and arid elevated topography region from Early Cretaceous (Horton et al., 2004). This may be a reason for the low exhumation rate in the Southern Qiangtang terrane, Tibet. Slope steepness is another factor that affects the erosional rates, that steep slope facilitates runoff and removal of sediments and results in intense erosion (Willgoose et al., 1991; Sillitoe, 2005). However, there is no deep incisely valley in central-western Tibet, and the slope in Duolong district is low. Additionally, uplift of Tibet is slow before ~100 Ma, and gradual after India-Asia collision (~55 Ma), and the abrupt uplift of Tibetan plateau happened more recently at ~7 Ma (Wang et al., 2008). Therefore, the

arid environment, slow uplift history, and relatively flat plateau in central-western Tibet during Early Cretaceous are combined to explain the slow exhumation rate of the Tiegelongnan deposit.

The magmatic-hydrothermal events at Tiegelongnan lasted from ~120 Ma to ~100 Ma, during several discontinuous pulses throughout about 20 million years. Porphyry stage intrusions, sericite alteration, and Cu-Mo mineralization (120 Ma), are overprinted by multiple stages of epithermal advanced argillic alteration and high-sulfidation Cu mineralization (116 Ma and 112 Ma). Most of the younger ages hydrothermal alteration and mineralization events lack associated porphyry intrusions. This long life-span at the Tiegelongnan deposit may be a result of the long-lasting tectonic active Bangong-Nujiang suture zone. At the regional scale, two generations of igneous rocks intruded during the Jurassic and Cretaceous near the subduction zone of the Bangong-Nujiang Oceanic (BNO) plate and subsequent collision between the Qiangtang and Lhasa terranes from 160 to 90 Ma (Li et al., 2014; Zhu et al., 2016). Several porphyry-related hydrothermal deposits surround the suture zone formed associated with magma related to the tectonic movement of BNO (Li et al., 2017a). Although it is uncertain the Duolong porphyry district formed during the subduction stage or collision stage, both subduction and post-subduction settings are favorable to the formation of porphyry and epithermal deposits (Richards, 2009; Hou et al., 2015).

Some high-sulfidation epithermal Au-Ag deposits formed simultaneously with associated porphyry events. For example, the alunite in Lepanto formed contemporaneously with the biotite in potassic alteration in the Far South-East porphyry deposit (Arribas et al., 1995). However, different types of alunite formed during discrete hydrothermal events in the epithermal Au-Ag deposit (Rye, 1993; Deyell et al., 2005a). Advanced argillic alteration and associated high-sulfidation mineralization are believed to be repetitive in porphyry-related districts (Hervé et al., 2012; Sillitoe et al., 2019). In some examples, alunite from epithermal deposits is younger than the associated porphyry deposits. Porphyry Cu-Mo mineralization in La Bodega and La Mascota deposits, Colombia formed at 10.1 Ma, before epithermal Au-Ag-Cu mineralization at 2.6 Ma and Zn mineralization 1.6 Ma (Madrid et al., 2017). Epithermal Cu-Ag sulfide veins in Collahuasi District formed at 32.7 Ma, which is younger than porphyry Cu-Mo mineralization at 34.4 Ma (Masterman et al., 2004).

10. Conclusions

The Tiegelongnan porphyry-epithermal Cu deposit in the Duolong porphyry district at the Bangong-Nujiang suture zone, Tibet, China, is hosted by Jurassic sedimentary rocks, and was emplaced during several pulses of Cretaceous granodiorite porphyry intrusions at ~120 and ~116 Ma. The porphyry alteration and mineralization are genetically related to the ~120 Ma porphyry intrusions. Epithermal advanced argillic alteration and high sulfidation Cu mineralization took place mainly at ~116 Ma and ~112 Ma, which telescopes the earlier porphyry hydrothermal system.

The top of the porphyry and epithermal hydrothermal alteration and mineralization system were partly unroofed. Continuing supergene weathering, uplift, and erosion along with the formation of the Tiegelongnan deposit lasted for around 10 million years until covered by andesite at ~110 Ma. The andesite cover is of great significance to preserving this deposit, and it may be associated with weak hydrothermal alteration. The long-lasting magmatic-hydrothermal formation processes are attributed to the prolonged active convergent plate margin at the Bangong-Nujiang Suture. The geochronology data reveal a long duration (~10 m. y) slow exhumation history, much longer than the reported rapid exhumation process < 2 m. y. in other regions, which is like due to the combination of arid environment, flat plateau, and slow uplift process in the central-western Tibet during Early Cretaceous.

After the burial under the andesite, the Tiegelongnan deposit is continually subjected to exhumation and supergene oxidation, which outcrop the Tiegelongnan porphyry-epithermal system, widen and deepen oxidation zone, and form supergene enrichment.

Declaration of Competing Interest

The authors declare that they have no known competing financial interests or personal relationships that could have appeared to influence the work reported in this paper.

Acknowledgments

This work is jointed sponsored by the Public Science and Technology Research Funds Projects, National Key R&D Program of China, Deep Resources Exploration and Mining (No. 2018YFC0604106), and Basic Research Fund of the Chinese Academy of Geological Sciences (No. YYWF201608). The first author's doctoral study and living in Université Laval, Canada is sponsored by the China Scholarship Council. G. Beaudoin acknowledges NSERC for its long term support. We thank Chinalco Jinlong Company for supporting our fieldwork and permission for access to the cores. Yiyun Wang, Huanhuan Yang, Ke Gao, Shuai Ding, and Junlong Song are thanked for their assisting with core logging, photographing, and sample collection. We acknowledge Richard Friedman and Janet Gabites (University of British Columbia) for their help with the careful zircon CA-ID-TIMS dating, and muscovite and alunite Ar-Ar dating and data interpretation respectively, Geng Jianzhen (Tianjin Geological Survey) for his help with zircon LA-ICP-MS dating. Xiaowen Huang and Bertrand Rottier offered detailed reviews and comments, that helped improve the manuscript draft. We thank two anonymous reviewers for their insightful comments, Associate Editor Taofa Zhou, and Editor Franco Pirajno for their helpful editorial comments.

Appendix A. Supplementary data

Supplementary data to this article can be found online at https://doi.org/10.1016/j.oregeorev.2020.103575.

References

Arribas, A., Hedenquist, J.W., Itaya, T., Okada, T., Concepción, R.A., Garcia, J.S., 1995. Contemporaneous formation of adjacent porphyry and epithermal Cu-Au deposits over 300 ka in northern Luzon, Philippines. Geology 23 (4), 337–340.

Arribas Jr, A., 1995. Characteristics of high-sulfidation epithermal deposits, and their relation to magmatic fluid. Mineral. Assoc. Canada Short Course 23, 419–454.

Braxton, D.P., Cooke, D.R., Ignacio, A.M., Waters, P.J., 2018. Geology of the Boyongan and Bayugo porphyry Cu-Au deposits: an emerging porphyry district in northeast Mindanao, Philippines. Econ. Geol. 113 (1), 83–131.

Catchpole, H., Kouzmanov, K., Bendezú, A., Ovtcharova, M., Spikings, R., Stein, H., Fontboté, L., 2015. Timing of porphyry (Cu-Mo) and base metal (Zn-Pb-Ag-Cu) mineralisation in a magmatic-hydrothermal system—Morococha district, Peru. Miner. Deposita 50 (8), 895–922.

Cathles, L., Shannon, R., 2007. How potassium silicate alteration suggests the formation of porphyry ore deposits begins with the nearly explosive but barren expulsion of large volumes of magmatic water. Earth Planet. Sci. Lett. 262 (1–2), 92–108.

Cathles, L.M., Erendi, A., Barrie, T., 1997. How long can a hydrothermal system be sustained by a single intrusive event? Econ. Geol. 92 (7–8), 766–771.

Chiaradia, M., Schaltegger, U., Spikings, R., Wotzlaw, J.-F., Ovtcharova, M., 2013. How accurately can we date the duration of magmatic-hydrothermal events in porphyry systems?—an invited paper. Econ. Geol. 108 (4), 565–584.

Chouinard, A., Williams-Jones, A.E., Leonardson, R.W., Hodgson, C.J., Silva, P., Téllez, C., Vega, J., Rojas, F., 2005. Geology and genesis of the multistage high-sulfidation epithermal Pascua Au-Ag-Cu deposit, Chile and Argentina. Econ. Geol. 100 (3), 463–490.

Cooke, D.R., Simmons, S.F., 2000. Characteristics and genesis of epithermal gold deposits. Rev. Econ. Geol. 13, 221–244.

Correa, K.J., Rabbia, O.M., Hernández, L.B., Selby, D., Astengo, M., 2016. The timing of magmatism and ore formation in the El Abra porphyry copper deposit, northern Chile: implications for long-lived multiple-event magmatic-hydrothermal porphyry systems. Econ. Geol. 111 (1), 1–28.

Deyell, C., Leonardson, R., Rye, R., Thompson, J., Bissig, T., Cooke, D., 2005a. Alunite in the Pascua-Lama high-sulfidation deposit: constraints on alteration and ore deposition using stable isotope geochemistry. Econ. Geol. 100 (1), 131–148.

Deyell, C., Rye, R., Landis, G., Bissig, T., 2005b. Alunite and the role of magmatic fluids in the Tambo high-sulfidation deposit, El Indio-Pascua belt, Chile. Chem. Geol. 215 (1), 185–218.
Ding, S., Chen, Y., Tang, J., Zheng, W., Lin, B., Yang, C., 2017. Petrogenesis and Tectonics of the Naruo Porphyry Cu (Au) Deposit Related Intrusion in the Duolong Area, Central Tibet. Acta Geol. Sin. (English Edition) 91 (2), 581–601.
Fang, X., Tang, J., Song, Y., Yang, C., Ding, S., Wang, Y.-Y., Wang, Q., Sun, X.-G., Li, Y.-B., Wei, L.-J., 2015. Formation epoch of the South Tiegelong superlarge epithermal Cu (Au-Ag) deposit in Tibet and its geological implications. Acta Geosci. Sin. 36 (2), 168–176.
Fontboté, L., Bendezú, R., 2009. Cordilleran or Butte-type veins and replacement bodies as a deposit class in porphyry systems:. In: Proceedings of the 10th Biennial Society of Geology Applied to Ore Deposits Meeting, Townsville, Australia, pp. 521–523.
Garwin, S., Hall, R., Watanabe, Y., 2005. Tectonic setting, geology, and gold and copper mineralization in Cenozoic magmatic arcs of Southeast Asia and the West Pacific. Econ. Geol. 100th Anniversary Volume 891–930.
Geng, J.-Z., Zhang, J., Li, H.-K., Li, H.-M., Zhang, Y.-Q., Hao, S., 2012. Ten-micron-sized zircon U-Pb dating using LA-MC-ICP-MS. Diqiu Xuebao(Acta Geoscientica Sinica) 33 (6), 877–884.
Gray, J.E., Coolbaugh, M.F., 1994. Geology and geochemistry of Summitville, Colorado: an epithermal acid sulfate deposit in a volcanic dome. Econ. Geol. 89, 18.
Guo, N., Tong, Q.-X., Wang, C., Tang, N., Fu, Y., 2017. Alteration mapping and prospecting model construction at Tiegelongnan, Duolong metallogenic district, northern Tibet, as revealed by shortwave infrared technique. Geol. Bull. China (in Chinese) 37 (2/3), 446–457.
Gustafson, L.B., Hunt, J.P., 1975. The porphyry copper deposit at El Salvador, Chile. Econ. Geol. 70 (5), 857–912.
Hedenquist, J.W., Arribas, A., Gonzalez-Urien, E., 2000. Exploration for epithermal gold deposits. Rev. Econ. Geol. 13, 245–277.
Hedenquist, J.W., Arribas, A.J., Reynolds, T.J., 1998. Evolution of an intrusion-centered hydrothermal system Far Southeast-Lepanto porphyry and epithermal Cu-Au Deposits, Philippine. Econ. Geol. 93, 373–404.
Hervé, M., Sillitoe, R., Wong, C., Fernández, P., Crignola, F., Ipinza, M., Urzúa, F., Hedenquist, J., Harris, M., Camus, F., 2012. Geologic overview of the Escondida porphyry copper district, northern Chile. Soc. Econ. Geol. Special Publication 16, 55–78.
Horton, B.K., Dupont-Nivet, G., Zhou, J., Waanders, G., Butler, R.F., Wang, J., 2004. Mesozoic-Cenozoic evolution of the Xining-Minhe and Dangchang basins, northeastern Tibetan Plateau: magnetostratigraphic and biostratigraphic results. J. Geophys. Res.: Solid Earth 109 (B04402).
Hou, Z., Yang, Z., Lu, Y., Kemp, A., Zheng, Y., Li, Q., Tang, J., Yang, Z., Duan, L., 2015. A genetic linkage between subduction-and collision-related porphyry Cu deposits in continental collision zones. Geology 43 (3), 247–250.
Hou, Z., Zhang, H., Pan, X., Yang, Z., 2011. Porphyry Cu (–Mo–Au) deposits related to melting of thickened mafic lower crust: examples from the eastern Tethyan metallogenic domain. Ore Geol. Rev. 39 (1), 21–45.
Jansen, N.H., Gemmell, J.B., Chang, Z., Cooke, D.R., Jourdan, F., Creaser, R.A., Hollings, P., 2017. Geology and genesis of the Cerro la Mina porphyry-high sulfidation Au (Cu-Mo) Prospect Mexico. Econ. Geol. 112 (4), 799–827.
Jiang, S.-H., Liang, Q.-L., Bagas, L., Wang, S.-H., Nie, F.-J., Liu, Y.-F., 2013. Geodynamic setting of the Zijinshan porphyry–epithermal Cu–Au–Mo–Ag ore system, SW Fujian Province, China: constrains from the geochronology and geochemistry of the igneous rocks. Ore Geol. Rev. 53, 287–305.
Kesler, S.E., Wilkinson, B.H., 2006. The role of exhumation in the temporal distribution of ore deposits. Econ. Geol. 101 (5), 919–922.
Li, G.-M., Qin, K.-Z., Li, J.-X., Evans, N.J., Zhao, J.-X., Cao, M.-J., Zhang, X.-N., 2017a. Cretaceous magmatism and metallogeny in the Bangong-Nujiang metallogenic belt, central Tibet: evidence from petrogeochemistry, zircon U-Pb ages, and Hf–O isotopic compositions. Gondwana Res. 41, 110–127.
Li, G., Li, J., Qin, K., Duo, J., Zhang, T., Xiao, B., Zhao, J., 2012. Geology and hydrothermal alteration of the duobuza gold-rich porphyry copper District in the Bangongco Metallogenetic Belt, Northwestern Tibet. Resour. Geol. 62 (1), 99–118.
Li, J.-X., Qin, K.-Z., Li, G.-M., Evans, N.J., Zhao, J.-X., Cao, M.-J., Huang, F., 2016a. The Nadun Cu–Au mineralization, central Tibet: root of a high sulfidation epithermal deposit. Ore Geol. Rev. 78, 371–387.
Li, J., Qin, K., Li, G., Xiao, B., Zhao, J., Chen, L., 2011. Magmatic-hydrothermal evolution of the Cretaceous Duolong gold-rich porphyry copper deposit in the Bangongco metallogenic belt, Tibet: evidence from U-Pb and 40 Ar/39 Ar geochronology. J. Asian Earth Sci. 41 (6), 525–536.
Li, J.X., Qin, K.Z., Li, G.M., Richards, J.P., Zhao, J.X., Cao, M.J., 2014. Geochronology, geochemistry, and zircon Hf isotopic compositions of Mesozoic intermediate–felsic intrusions in central Tibet: petrogenetic and tectonic implications. Lithos 198–199, 77–91.
Li, J.X., Qin, K.Z., Li, G.M., Xiao, B., Zhao, J.X., Cao, M.J., Chen, L., 2013. Petrogenesis of ore-bearing porphyries from the Duolong porphyry Cu–Au deposit, central Tibet: evidence from U-Pb geochronology, petrochemistry and Sr–Nd–Hf–O isotope characteristics. Lithos 160, 216–227.
Li, J.X., Qin, K.Z., Li, G.M., Xiao, B., Zhao, J.X., Chen, L., 2016b. Petrogenesis of Cretaceous igneous rocks from the Duolong porphyry Cu–Au deposit, central Tibet: evidence from zircon U-Pb geochronology, petrochemistry and Sr–Nd–Pb–Hf isotope characteristics. Geol. J. 51 (2), 285–307.
Li, S., Yin, C., Guilmette, C., Ding, L., Zhang, J., 2019. Birth and demise of the Bangong-Nujiang Tethyan Ocean: a review from the Gerze area of central Tibet. Earth-Sci. Rev. 198 (102907).
Li, X.K., Li, C., Sun, Z.M., Wang, M., 2017b. Origin and tectonic setting of the giant Duolong Cu–Au deposit, South Qiangtang Terrane, Tibet: evidence from geochronology and geochemistry of Early Cretaceous intrusive rocks. Ore Geol. Rev. 80, 61–78.
Lin, B., Chen, Y., Tang, J., Wang, Q., Song, Y., Yang, C., Wang, W., He, W., Zhang, L., 2017a. 40Ar/39Ar and Rb-Sr Ages of the Tiegelongnan Porphyry Cu-(Au) Deposit in the Bangong Co-Nujiang Metallogenic Belt of Tibet, China: implication for Generation of Super-Large Deposit. Acta Geol. Sin. (English Edition) 91 (2), 602–616.
Lin, B., Tang, J., Chen, Y., Baker, M., Song, Y., Yang, H., Wang, Q., He, W., Liu, Z., 2018. Geology and geochronology of Naruo large porphyry-breccia Cu deposit in the Duolong district, Tibet. Gondwana Res. 66, 168–182.
Lin, B., Tang, J.X., Chen, Y.C., Song, Y., Hall, G., Wang, Q., Yang, C., Fang, X., Duan, J., Yang, H.H., 2017b. Geochronology and genesis of the tiegelongnan porphyry Cu (Au) deposit in Tibet: evidence from U-Pb, Re–Os dating and Hf, S, and H–O isotopes. Resour. Geol. 67 (1), 1–21.
Liu, D., Shi, R., Ding, L., Huang, Q., Zhang, X., Yue, Y., Zhang, L., 2015. Zircon U–Pb age and Hf isotopic compositions of Mesozoic granitoids in southern Qiangtang, Tibet: implications for the subduction of the Bangong–Nujiang Tethyan Ocean: Gondwana Research.
Liu, Y., Wang, M., Li, C., Xie, C., Chen, H., Li, Y., Fan, J., Li, X., Xu, W., Sun, Z., 2017. Cretaceous structures in the Duolong region of central Tibet: evidence for an accretionary wedge and closure of the Bangong-Nujiang Neo-Tethys Ocean. Gondwana Res. 48, 110–123.
Madrid, A.L.R., Bissig, T., Hart, C.J., Figueroa, L.C.M., 2017. Late pliocene high-sulfidation epithermal gold mineralization at the La Bodega and La Mascota deposits, Northeastern Cordillera of Colombia. Econ. Geol. 112 (2), 347–374.
Mao, J., Pirajno, F., Lehmann, B., Luo, M., 2014. Berzina, ADistribution of porphyry deposits in the Eurasian continent and their corresponding tectonic settings. J. Asian Earth Sci. 79, 576–584.
Masterman, G.J., Cooke, D.R., Berry, R.F., Clark, A.H., Archibald, D.A., Mathur, R., Walshe, J.L., Durán, M., 2004. 40Ar/39Ar and Re-Os geochronology of porphyry copper-molybdenum deposits and related copper-silver veins in the Collahuasi district, northern Chile. Econ. Geol. 99 (4), 673–690.
Maydagán, L., Franchini, M., Chiaradia, M., Dilles, J., Rey, R., 2014. The Altar porphyry Cu-(Au-Mo) deposit (Argentina): a complex magmatic-hydrothermal system with evidence of recharge processes. Econ. Geol. 109 (3), 621–641.
McInnes, B. I., Evans, N. J., Fu, F., Garwin, S., Belousova, E., Griffin, W., Bertens, A., Sukarna, D., Permanadewi, S., Andrew, R., 2005. Thermal history analysis of selected Chilean, Indonesian, and Iranian porphyry Cu-Mo-Au deposits. In: Porter, T.M. (Ed.), Super Porphyry Copper and Gold Deposits. A Global Perspective. Porter Geoconsultancy Publishing, de Adelaide, Australia, pp. 27–42.
Mercer, C.N., Reed, M.H., Mercer, C.M., 2015. Time scales of porphyry cu deposit formation: insights from titanium diffusion in quartz. Econ. Geol. 110 (3), 587–602.
Parry, W., Wilson, P.N., Moser, D., Heizler, M.T., 2001. U-Pb dating of zircon and 40Ar/39Ar dating of biotite at Bingham, Utah. Econ. Geol. 96 (7), 1671–1683.
Perelló, J., Cox, D., Garamjav, D., Sanjdorj, S., Diakov, S., Schissel, D., Munkhbat, T.-O., Oyun, G., 2001. Oyu Tolgoi, Mongolia: siluro-devonian porphyry Cu-Au-(Mo) and high-sulfidation Cu mineralization with a cretaceous chalcocite blanket. Econ. Geol. 96 (6), 1407–1428.
Richards, J.P., 2009. Postsubduction porphyry Cu-Au and epithermal Au deposits: products of remelting of subduction-modified lithosphere. Geology 37 (3), 247–250.
Rye, R.O., 1993. The evolution of magmatic fluids in the epithermal environment; the stable isotope perspective. Econ. Geol. 88 (3), 733–752.
Scoates, J.S., Friedman, R.M., 2008. Precise age of the platiniferous Merensky Reef, Bushveld Complex, South Africa, by the U-Pb zircon chemical abrasion ID-TIMS technique. Econ. Geol. 103 (3), 465–471.
Seedorff, E., Dilles, J., Proffett, J., Einaudi, M., Zurcher, L., Stavast, W., Johnson, D., Barton, M., 2005. Porphyry deposits: characteristics and origin of hypogene features. Econ. Geol. 100th Anniv. 29, 251–298.
Sillitoe, R.H., 1999. Styles of High-Sulphidation Gold,Silver and Copper Mineralisation in Porphyry and Epithermal Environments. In: Weber, G. (Ed.), Pacrim '99 Congress, Bali, Indonesia, 1999, Proceedings: Parkville, Australasian Institute of Mining and Metallurgy, pp. 29–44.
Sillitoe, R.H., 2005. Supergene oxidized and enriched porphyry copper and related deposits. Econ. Geol. 100, 723–768.
Sillitoe, R.H., 2010. Porphyry copper systems. Econ. Geol. 105, 3–41.
Sillitoe, R.H., Devine, F.A.M., Sanguinetti, M.I., Friedman, R.M., 2019. Geology of the Josemaría Porphyry Copper-Gold Deposit, Argentina: formation, exhumation, and burial in two million years. Econ. Geol. 114 (3), 407–426.
Sillitoe, R.H., Hedenquist, J.W., 2003. Linkages between volcanotectonic settings, ore-fluid compositions, and epithermal precious metal deposits. Special Publication-Soc. Econ. Geol. 10, 315–343.
Sillitoe, R.H., Moretensen, J.K., 2010. Longevity of porphyry copper formation at Quellaveco, Peru. Econ. Geol. 106, 1157–1162.
So, C.-S., Dequan, Z., Yun, S.-T., Daxing, L., 1998. Alteration-mineralization zoning and fluid inclusions of the high sulfidation epithermal Cu-Au mineralization at Zijinshan, Fujian Province, China. Econ. Geol. 93 (7), 961–980.
Song, Y., Yang, C., Wei, S., Yang, H., Fang, X., Lu, H., 2018. Tectonic control, reconstruction and preservation of the tiegelongnan porphyry and epithermal overprinting Cu (Au) deposit, Central Tibet, China. Minerals 8 (9), 398–415.
Song, Y., Yang, H., Lin, B., Liu, Z., Qin, W., Ke, G., Chao, Y., Xiang, F., 2017. The preservation system of epithermal deposits in South Qiangtang terrane of central Tibetan Plateau and its significance: a case study of the Tiegelongnan superlarge deposit. Acta Geosci. Sin. 38, 659–669.
Stoffregen, R.E., 1987. Genesis of acid-sulfate alteration and Au-Cu-Ag mineralization at Summitville, Colorado. Econ. Geol. 82, 1575–1591.
Sun, J., Mao, J., Beaudoin, G., Duan, X., Yao, F., Ouyang, H., Wu, Y., Li, Y., Meng, X., 2017. Geochronology and geochemistry of porphyritic intrusions in the Duolong

porphyry and epithermal Cu-Au district, central Tibet: implications for the genesis and exploration of porphyry copper deposits. Ore Geol. Rev. 80, 1004–1019.
Tang, J.-X., Liu, H.-F., Lang, X.-H., Zhang, J.-S., Zheng, W.-B., Ying, L.-J., 2012. Minerogenetic series of ore deposits in the east part of the Gangdise metallogenic belt. Diqiu Xuebao (Acta Geoscientica Sinica) 33 (4), 393–410.
Tang, J.-X., Wang, Q., Yang, H.-H., Gao, X., Zhang, Z.-B., Zou, B., 2017. Mineralization, exploration and resource potential of porphyry-skarn-epithermal copper polymetallic deposits in Tibet. Acta Geoscientica Sinica 38 (5), 571–613.
Tang, J., Sun, X., Ding, S., Wang, Q., Wang, Y., Yang, C., Chen, H., Li, Y., Li, Y., Wei, L., 2014. Discovery of the epithermal deposit of Cu (Au-Ag) in the Duolong ore concentrating area, Tibet. Acta Geosci. Sin. 35, 6–10.
Wainwright, A.J., Tosdal, R.M., Lewis, P.D., Friedman, R.M., 2017. Exhumation and preservation of porphyry Cu-Au deposits at Oyu Tolgoi, South Gobi Region, Mongolia. Econ. Geol. 112 (3), 591–601.
Wang, C., Zhao, X., Liu, Z., Lippert, P.C., Graham, S.A., Coe, R.S., Yi, H., Zhu, L., Liu, S., Li, Y., 2008. Constraints on the early uplift history of the Tibetan Plateau. Proc. Natl. Acad. Sci. 105 (13), 4987–4992.
Wang, Q., Juxing, T., Xiang, F., Bin, L., Yang, S., Yiyun, W., Huanhuan, Y., Chao, Y., Yanbo, L., Lujie, W., 2015. Petrogenetic setting of andsites in Rongna ore block, Tiegelong Cu (Au–Ag) deposit, Duolong ore concentration area, Tibet: evidence from zircon U-Pb LA–ICP–MS dating and petrogeochemistry of andsites. Geol. China 42 (5), 1324–1336.
Wei, S.-G., Tang, J.-X., Song, Y., Liu, Z.-B., Feng, J., Li, Y.-B., 2017. Early Cretaceous bimodal volcanism in the Duolong Cu mining district, western Tibet: record of slab breakoff that triggered ca. 108–113 Ma magmatism in the western Qiangtang terrane. J. Asian Earth Sci. 138, 588–607.
Willgoose, G., Bras, R.L., Rodriguez-Iturbe, I., 1991. Results from a new model of river basin evolution. Earth Surf. Proc. Land. 16 (3), 237–254.
Yang, C., Tang, J., Wang, Y., Yang, H., Wang, Q., Sun, X., Feng, J., Yin, X., Ding, S., Fang, X., 2014. Fluid and geological characteristics researches of Southern Tiegelong epithermal porphyry Cu-Au deposit in Tibet. Miner. Deposits 33, 1287–1305.
Yanites, B.J., Kesler, S.E., 2015. A climate signal in exhumation patterns revealed by porphyry copper deposits. Nat. Geosci. 8 (6), 462–466.
Zhang, X.-N., Li, G.-M., Qin, K.-Z., Lehmann, B., Li, J.-X., Zhao, J.-X., Cao, M.-J., Zou, X.-Y., 2018. Petrogenesis and tectonic setting of Early Cretaceous granodioritic porphyry from the giant Rongna porphyry Cu deposit, central Tibet. J. Asian Earth Sci. 161, 74–92.
Zhang, Z., Xiang, F., JuXing, T., Qin, W., Chao, Y., YiYun, W., Shuai, D., HuanHuan, Y., 2017. Chronology, geochemical characteristics of the Gaerqin porphyry copper deposit in the Duolong ore concentration area in Tibet and discussion about the identification of the lithoscaps and the possible epithermal deposit. Acta Petrologica Sinica 33 (2), 476–494.
Zhu, D.-C., Li, S.-M., Cawood, P.A., Wang, Q., Zhao, Z.-D., Liu, S.-A., Wang, L.-Q., 2016. Assembly of the Lhasa and Qiangtang terranes in central Tibet by divergent double subduction. Lithos 245, 7–17.
Zhu, X., Li, G., Chen, H., Ma, D., Huang, H., 2015. Zircon U-Pb, Molybdenite Re-Os and K-feldspar 40Ar/39Ar dating of the Bolong Porphyry Cu-Au deposit, Tibet, China. Resour. Geol. 65 (2), 122–135.